

Effects of seasonal variations in vegetation and precipitation on catchment erosion rates along a climate and ecological gradient: Insights from numerical modelling

Hemanti Sharma¹ and Todd A. Ehlers^{1,2}

¹Department of Geosciences, University of Tübingen, Schnarrenbergstr. 94-96, 72076, Germany

²School of Geographical and Earth Sciences, University of Glasgow, Glasgow, Scotland

Correspondence to: Todd A. Ehlers (todd.ehlers@uni-tuebingen.de)

Abstract. Precipitation in wet seasons influences catchment erosion and contributes to annual erosion rates. However, wet seasons are also associated with increased vegetation cover, which helps resist erosion. This study investigates the effect of present-day seasonal variations in rainfall and vegetation cover on erosion rates for four catchments along the extreme climate and ecological gradient (from arid to temperate) of the Chilean Coastal Cordillera (~26 °S – ~38 °S). We do this using the Landlab-SPACE landscape evolution model using a set of runtime scripts and input files to account for vegetation-dependent hillslope-fluvial processes and hillslope hydrology. Model inputs include present-day (90 m) topography, and a timeseries (from 2000-2019) of MODIS-derived NDVI for vegetation seasonality; weather station observations of precipitation; and evapotranspiration obtained from GLDAS NOAH. Simulations were conducted with a step-wise increase in complexity to quantify the sensitivity of catchment scale erosion rates to seasonal average variations in precipitation and/or vegetation cover. Simulations were conducted for 1,000 years (20 years of vegetation and precipitation observations repeated 50 times). After detrending the results for long-term transient changes, the last 20 years were analyzed. Results indicate that when vegetation cover is variable but precipitation is held constant, the amplitude of change in erosion rates relative to mean erosion rates ranges between 5% (arid) to 36% (Mediterranean setting). In contrast, in simulations with variable precipitation change and constant vegetation cover, the amplitude of change in erosion rates is higher and ranges between 13% (arid) to 91% (Mediterranean setting). Finally, simulations with coupled precipitation and vegetation cover variations demonstrate variations in catchment erosion of 13% (arid) to 97% (Mediterranean setting). Taken together, we find that precipitation variations more strongly influence seasonal variations in erosion rates. However, the effects of seasonal variations in vegetation cover on erosion are also significant (between 5-36%) and are most pronounced in semi-arid to Mediterranean settings and least prevalent in arid and humid-temperature settings.

Keywords: Landlab, vegetation, Chilean Coastal Cordillera, biogeomorphology, seasonality, precipitation, EarthShape.

1 Introduction

Catchment erosion rates vary spatially and temporally (e.g., Wang et al., 2021) and depend on topography (slope, Carretier et al., 2018), vegetation cover and type (e.g., Zhang et al., 2011; Starke et al., 2020; Schaller and Ehlers, 2022) and precipitation rates (e.g., Cerdà, 1998; Tucker and Bras, 2000). Over annual timescales, temporal variations in catchment erosion occur in response to seasonal variations in precipitation and vegetation cover. For example, previous work has found that a significant fraction of annual erosion occurs during wet seasons, with high runoff rates (Hancock and Lowry, 2021; Leyland et al., 2016; Gao et al., 2021; Wulf et al., 2010). However, this increase in precipitation during wet seasons also promotes vegetation growth, which in turn influences erosion rates (Langbein and Schumm, 1958; Zheng, 2006; Schmid et al., 2018). Seasonal and longer-term changes in both precipitation and vegetation cover play a crucial role in intra-annual changes in erosion rates (Istanbulluoglu and Bras, 2006; Yetemen et al., 2015; Schmid et al., 2018; Sharma et al., 2021). The intensity, frequency, and seasonality of precipitation and vegetation cover change within a year depend upon the climate and ecological conditions of

39 the area of interest (Herrmann and Mohr, 2011). One means of investigating the effects of seasonality in precipitation and (or)
40 vegetation cover on erosion rates is through landscape evolution modeling (LEM), which can be parameterized for variations
41 in vegetation-dependent hillslope and fluvial processes over seasonal time scales.

42 Previous modeling and observational studies have investigated the effects of seasonality in precipitation and vegetation on
43 catchment erosion. Bookhagen et al., (2005), Wulf et al., (2010), and Deal et al., (2017) investigated the effects of stochastic
44 variations in precipitation on erosion and sediment transport in the Himalayas. They found that high variability in rainstorm
45 days (>80% of MAP) during the wet season (summer monsoon) caused high variability in the suspended sediment load. Similar
46 seasonality in sediment loads was reported in a field study in Iran, using sediment traps and erosion pins. These authors
47 concluded that wet seasons experienced maximum erosion rates (>70% of annual), which decreased in dry seasons (<10% of
48 annual) (Mosaffaie et al., 2015). Field observations in the heavily vegetated Columbian Andes concluded that soil erosion and
49 nutrient losses are significantly influenced by precipitation seasonality (Suescún et al., 2017). In contrast, work by Steegen et
50 al., (2000) in a loamy agricultural catchment in central Belgium found suspended sediment concentrations in streams were
51 lower during summer (wet) rather than winter (dry) months due to the development in vegetation cover in the wet season.
52 Other workers have found a dependence of seasonal erosion on ecosystem type. For example, Istanbuloglu et al., (2006)
53 found a reduction in the sensitivity of soil loss potential to storm frequency in humid ecosystems compared to arid and semi-
54 arid regions. Work by Wei et al., (2015) in the semi-arid setting of the Chinese Loess Plateau, reported that significant changes
55 in vegetation related land use/land cover may contribute to long-term soil loss dynamics. However, seasonal variations in
56 runoff and sediment yield are mainly influenced by intra-annual rainfall variations. Finally, previous work in a Mediterranean
57 environment by Gabarrón-Galeote et al., (2013), described rainfall intensity as the main factor in determining hydrological
58 erosive response, regardless of the rainfall depth of an event.

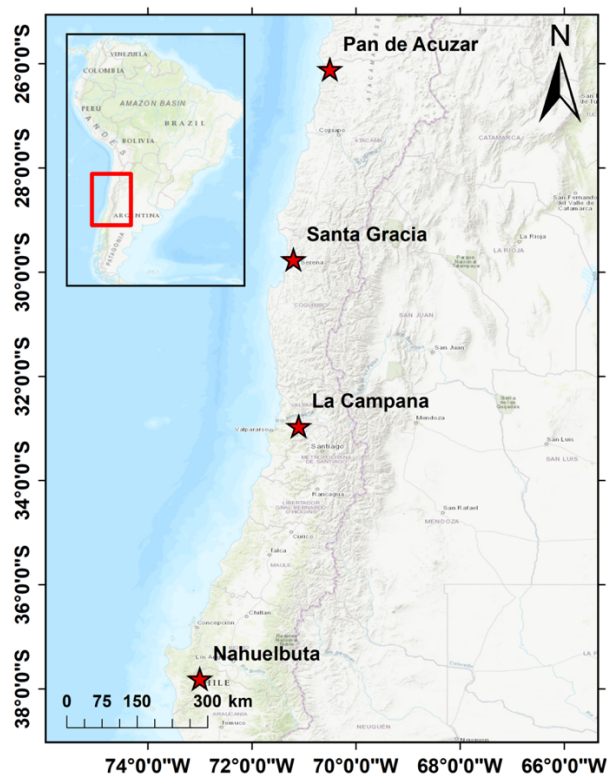
59 When looking at seasonal vegetation changes in more detail, several different studies suggest these changes are important for
60 catchment erosion. For example, Garatuza-Payán et al., (2005) emphasized that seasonal patterns in erosion are strongly
61 influenced by plant phenology as demonstrated by the changes in vegetation cover (measured by NDVI). A similar study on
62 the Loess Plateau, China, by Zheng (2006) documented decreasing soil erosion as vegetation cover increases during the wet
63 season. Work conducted in a forested setting (Zhang et al., 2014) documented the importance of tree cover as an effective
64 filter for decreasing the effects of rainfall intensity on soil structure, runoff, and sediment yield. Numerical modeling studies
65 have also found a significant impact of vegetation on erosion. For example, Zhang et al., (2019) found that when precipitation
66 was kept constant, the increase in vegetation cover resulted in a significant reduction in sediment yields (20-30% of the total
67 flux). Also, during early to mid-wet season, the species richness and evenness of plant cover both play an essential role in
68 reducing erosion rates during low rainfall events (Hou et al., 2020). However, in the case of high-intensity rainfall events at
69 the start of a wet season, when vegetation cover is low, the duration and intensity of rainfall were found to significantly affect
70 erosion rates (Hancock and Lowry, 2015). Other work conducted in a Mediterranean environment points to the coincidence of
71 peak rainfall erosivity in low vegetation cover settings, leading to an increased risk of soil erosion (Ferreira and Panagopoulos,
72 2014). Despite potentially conflicting results in the previous studies, what is clear is that seasonality in precipitation and
73 vegetation cover conspire to influence catchment erosion, although which factor (precipitation or vegetation) plays the
74 dominant role is unclear.

75 This study complements the previous work by applying a Landscape Evolution Model (LEM) to investigate seasonal transience
76 in catchment erosion due to variations in precipitation and vegetation. We do this for four locations spanning the extreme
77 climate and ecological gradient (i.e., arid, semi-arid, Mediterranean, and humid temperate) in the Chilean Coastal Cordillera.
78 Our efforts are focused on testing two hypotheses: (1) precipitation is the first-order driver of seasonal erosion rates, and (2)
79 catchment erosion in arid and semi-arid regions is more sensitive to seasonality in precipitation and vegetation than the
80 Mediterranean and humid temperate regions. To test the above hypotheses, we conduct a sensitivity analysis of fluvial and
81 hillslope erosion over four Chilean study areas to investigate the individual effects of seasonal changes in vegetation cover

82 and precipitation compared to simulations with coupled variations in precipitation and vegetation cover. We do this using a
83 two-dimensional LEM (the Landlab-SPACE software), which explicitly handles bedrock and sediment entrainment and
84 deposition. We build upon the approach of Sharma et al., (2021) with the additional consideration of soil-water infiltration.
85 Our model setup broadly representative of the present-day conditions in the Chilean Coastal Cordillera (Fig. 1) and uses
86 present-day inputs such as topography from SRTM DEMs (90 m) for four regions with different climate/ecological settings.
87 Simulations in these different ecosystems are driven by observed variations in vegetation cover from MODIS NDVI (between
88 2000 – 2019) and observed precipitation rates over the same time period from neighboring weather stations. We note that the
89 aim of this study is not to reproduce reality in these study areas. This is due to the uncertainties in the LEM initial conditions
90 and material properties, and rock uplift rates. Rather, our focus is a series of sensitivity analyses that are loosely ‘tuned’ to
91 natural conditions and observed vegetation and precipitation changes along an ecological gradient. As shown below, these
92 simplifications facilitate identifying the relative contributions of vegetation and precipitation changes on catchment erosion.

93 2 Study Areas

94 This section summarizes the geologic, climate, and vegetation settings of the four selected catchments (Fig. 1) investigated in
95 the Chilean Coastal Cordillera. These catchments (from north to south) are located in the Pan de Azúcar National Park (arid,
96 ~26°S), Santa Gracia Nature Reserve (semi-arid, ~30°S), and the La Campana (Mediterranean, ~33°S) and Nahuelbuta
97 (temperate-humid, ~38°S) national parks. Together, these study areas span ~1,300 km distance of the Coastal Cordillera. These
98 study areas are chosen for their steep climate and ecological gradient from north (arid environment with small to no shrubs) to
99 south (humid temperate environment with evergreen mixed forests) (Schaller et al., 2020). The study areas are part of the
100 German-Chilean priority research program EarthShape (www.earthshape.net) and ongoing research efforts within these
101 catchments.



102
103 **Figure 1. Study areas in the Coastal Chilean Cordillera ranging from an arid environment in the north (Pan de Azúcar),**
104 **semi-arid (Santa Gracia), Mediterranean (La Campana), and humid temperate environment in the south (Nahuelbuta).**
105 **The above map is obtained from the Environmental System Research Institute (ESRI) map server**
106 **(https://services.arcgisonline.com/ArcGIS/rest/services/World_Topo_Map/MapServer, last access: 25 April 2022).**

107 The bedrock of the four study areas is composed of granitoid rocks, including granites, granodiorites, and tonalites in Pan de
108 Azúcar, La Campana, and Nahuelbuta, respectively, and gabbro and diorites in Santa Gracia (Oeser et al., 2018). The soil
109 types in each catchment were identified as a sandy loam in three northern catchments (with high bulk density: 1300 – 1500 kg
110 m⁻³) and sandy clay loam in Nahuelbuta (with lower bulk density: 800 kg m⁻³) (Bernhard et al., 2018). The western margin of
111 Chile along the latitudes of the different study areas is characterized by a similar tectonic setting whereby an oceanic plate
112 (currently the Nazca Plate) has been subducting under the South American Plate since the Palaeozoic. Despite this common
113 tectonic setting along, slight differences in modern rock uplift rates are documented in the regions surrounding the three
114 northern catchments (i.e., < 0.1 mm yr⁻¹ for ~26 °S to ~33 °S) (Melnick, 2016) and the southern catchment (i.e., 0.04 to > 0.2
115 mm yr⁻¹ for ~38 °S over the last 4±1.2 Ma) (Glodny et al., 2008; Melnick et al., 2009). Over geologic (millennial) timescales,
116 measured denudation rates in the region range between ~0.005 to ~0.6 mm yr⁻¹ (Schaller et al., 2018). To facilitate a comparison
117 between the study areas and focus on erosion variations from seasonal changes in precipitation and vegetation, we assume a
118 uniform rock uplift rate of 0.05 mm yr⁻¹ for this study. This rate is broadly consistent with the range of previously reported
119 values.

120 The climate gradient in the study areas ranges from an arid climate in Pan de Azúcar (north) with mean annual precipitation
121 (MAP) of ~11 mm yr⁻¹ to semi-arid in Santa Gracia (MAP: ~88 mm yr⁻¹), a Mediterranean climate in La Campana (MAP:
122 ~350 mm yr⁻¹), and a temperate-humid climate in Nahuelbuta (south) with a MAP of 1400 mm yr⁻¹ (Ziese et al., 2020). The
123 observed mean annual temperatures (MAT) also vary with latitude ranging from ~20°C in the north to ~5°C in the south
124 (Übernicker et al., 2020). The previous gradients in MAP and MAT and latitudinal variations in solar radiation result in a
125 southward increase in vegetation density (Bernhard et al., 2018). The vegetation gradient is evident from mean MODIS
126 Normalized Difference Vegetation Index (NDVI) values range from ~0.1 in Pan de Azúcar (north) to ~0.8 in Nahuelbuta
127 (south) (Didan, Kamel, 2015). In this study, NDVI values are used as a proxy for vegetation cover density, similar to the
128 approach of Schmid et al. (2018). However, one of the major limitations of using NDVI is that the values get saturated when
129 the ground is covered by shrubs. This gradient in climate and vegetation cover from north to south in the Chilean Coastal
130 Cordillera provides an opportunity to study the effects of seasonal variations in vegetation cover and precipitation on
131 catchment-scale erosion rates in different environments.

132 **3 Methods**

133 This section comprises a description of model inputs (section 3.1), estimation of runoff rates (section 3.2), model setup (section
134 3.3), and initial and boundary conditions (section 3.4). This is followed by an overview of simulations conducted (section 3.5),
135 and a brief description of how detrending the model results was conducted to remove long-term transients (section 3.6).

136 **3.1 Data used for model inputs**

137 In contrast to previous modeling studies (Schmid et al., 2018; Sharma et al., 2021) in the same regions, we used present-day
138 topography as the initial condition for simulations instead of a synthetic topography produced during a model spin-up phase
139 in Landlab. This study focuses on predicting and comparing the average responses in catchment erosion that occur over
140 seasonal timescales with variable precipitation and vegetation cover. However, erosion in arid and semi-arid regions can vary
141 on sub-seasonal time scales due to high-intensity storms occurring over timescales of a couple of hours or days. Hence, the
142 model does not capture the role of extreme precipitation events. The effect of vegetation on erosion during extreme events is
143 the focus of ongoing work by the authors. Also, at seasonal time-steps, the relationship between vegetation cover and erosion
144 rates may be affected by inherited simulated slope values from the previous season, which may lead to the blended signal in
145 the output.

146 Initial topography for the four selected catchments was obtained by cropping the SRTM digital elevation model (DEM) in
 147 rectangular shapes encapsulating the catchment of interest (Fig. 1). These catchments are the same as those investigated with
 148 previous soil, denudation, and geophysical studies within the EarthShape project (e.g., Bernhard et al., 2018; Oeser et al., 2018;
 149 Schaller et al., 2018; Dal Bo et al., 2019). The DEM has a spatial resolution of 90 m and is the same as the cell size used in
 150 the model (dx and dy) (SRTM data set of Earth Resources Observation And Science (EROS) Center, 2017). The present-day
 151 total relief in the catchments are ~1852 m in La Campana (~33 °S), followed by ~1063 m in Santa Gracia (~30 °S), ~809 m in
 152 Nahuelbuta (~38 °S) and ~623 m Pan de Azúcar (~26 °S). Investigated catchment sizes considered here vary between ~64 km²
 153 in Pan de Azúcar, ~142.5 km² in Santa Gracia, ~106.8 km² in La Campana, and ~68.7 km² in Nahuelbuta. We note that present-
 154 day topography as the initial condition in simulations can introduce an initial transience in erosion rates due to assumed model
 155 erosional parameters (e.g., erodibility, hillslope diffusivity) differing from actual parameters within the catchment. We address
 156 this issue through a detrending of model results described later (see Section 3.6). Also, topography and processes represented
 157 by LEMs have inherent timescales that they respond to base on the physical properties used and model forcings (e.g., rock
 158 uplift), which are unknown. Hence, it is unlikely that the SRTM DEM used for the initial condition, is in equilibrium. Given
 159 this, the detrending of our time series of results to remove long-term transience aids in identifying seasonal transients in
 160 precipitation and vegetation cover.

161 Precipitation data applied over each study area (Fig. 3b) was acquired from the Global Precipitation Climatology Centre
 162 (GPCC) for the period 01/03/2000 to 31/12/2019 (DD/MM/YEAR). The data has a spatial resolution of 1° and a 1-day temporal
 163 resolution and comprises daily land-surface precipitation from rain gauges built on Global Telecommunication System-based
 164 and historic data (Ziese et al., 2020). The previous data was augmented with daily precipitation weather station data from
 165 01/02/2020 to 28/02/2020 obtained from Übernicker et al., (2020). We do this to include all the seasons between 2000 to 2019,
 166 i.e., from the austral autumn of 2000 to the austral summer of 2019. The periods (months of a year) of specific seasons in the
 167 Chilean Coastal Cordillera are given in Table 1. Seasonal precipitation rates were calculated by summing daily precipitation
 168 rates at three-month intervals. The seasonality and intensity of precipitation in the wet season (winter) increases from the arid
 169 (Pan de Azúcar) to humid temperate (Nahuelbuta) region.

170 **Table 1. Months of a year corresponding to specific seasons in the Chilean Coastal Cordillera**

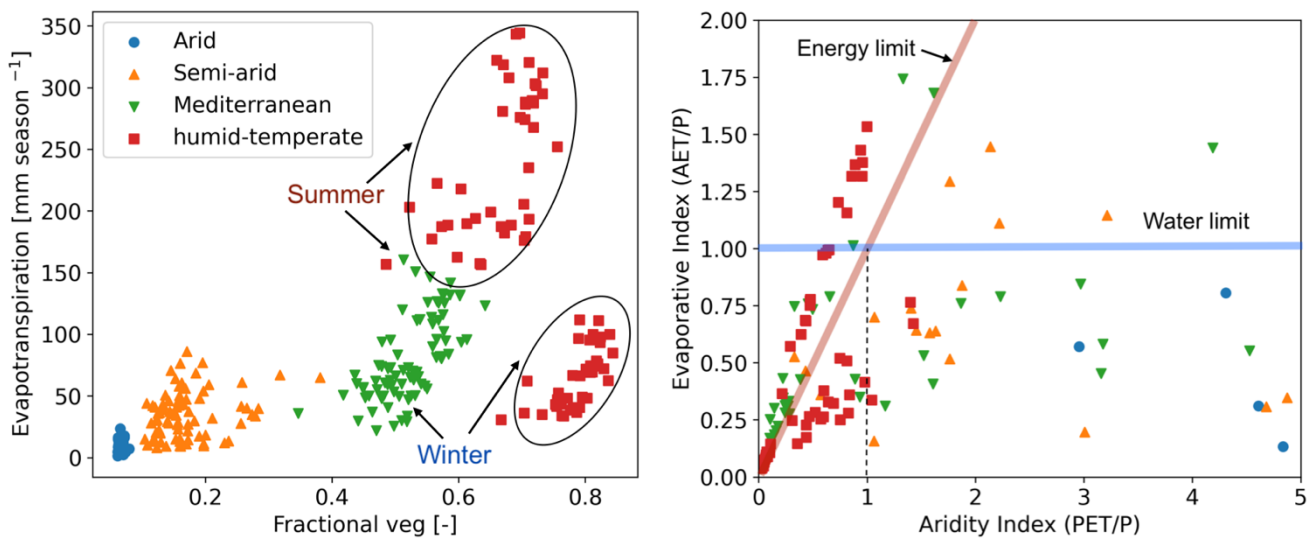
Seasons	Months
Summer ^{d*}	December - February
Autumn ^{w*}	March - May
Winter ^{w*}	June - August
Spring ^{d*}	September - November

171 *d: dry season, w: wet season
 172

173 NDVI derived from remote sensing imagery has been proven as an effective tool to estimate seasonal changes in vegetation
 174 cover density (Garatuza-Payán et al., 2005). Normalized difference vegetation index (NDVI) values were obtained from
 175 MODIS (Didan, Kamel, 2015) satellite data and were used as a proxy for changes in vegetation cover in the catchments.
 176 However, the major limitation of the conversion of NDVI to vegetation cover includes a saturation problem in NDVI values
 177 that occurs in high biomass regions such as our humid-temperate setting (Huete et al., 2002). This saturation can occur if the
 178 ground is covered by shrubs, at which point the information on different plant communities for associated erosion-relevant
 179 properties is lost (e.g., rooting depth, etc.). The NDVI data were acquired for 20 years (01/03/2000 – 28/02/2020), with a
 180 spatial resolution of 250 m and temporal resolution of 16 days. For application within the model simulations, the vegetation
 181 cover dataset was resampled using the nearest neighbour method to match the spatial resolution (90 m) of SRTM DEM and
 182 temporal resolution of 3 months. To summarize, season variations in precipitation rate and vegetation cover were applied to
 183 the simulations between 01/03/2000 and 28/02/2020 and encompass a 20-year record of observation variations in these factors.

184 Additional aspects of the catchment hydrologic cycle were determined using the following approaches for the same time period
 185 previously mentioned. First, evapotranspiration (ET) data was obtained from Global Land Data Assimilation System (GLDAS)
 186 Noah version 2.1, with a monthly temporal resolution and spatial resolution of 0.25° (~28 km) (Beaudoin et al., 2020; Rodell
 187 et al., 2004). The data was obtained from March-2000 to February-2020. Due to the coarse resolution of the dataset, ET is
 188 assumed to be uniform over the entire catchment area. No higher resolution datasets were available over the 20-year time-
 189 period of interest.

190 Soil properties such as the grain size distribution (sand, silt, and clay fraction) and bulk density were adapted from Bernhard
 191 et al., (2018) to estimate soil water infiltration capacity in each study area. Based on these soil properties, the soils have been
 192 classified as a sandy loam (in Pan de Azúcar, Santa Gracia, and La Campana) and sandy clay loam (Nahuelbuta). Average
 193 bulk density values of 1300 kg m⁻³, 1500 kg m⁻³, 1300 kg m⁻³, and 800 kg m⁻³ were used for Pan de Azúcar, Santa Gracia, La
 194 Campana, and Nahuelbuta, respectively (Bernhard et al., (2018).



195
 196 **Figure 2. Parameter correlation for observations used as model input data (i.e., seasonal precipitation, vegetation cover**
 197 **and evapotranspiration) including: (a) fractional vegetation cover (derived from NDVI) and evapotranspiration**
 198 **(derived from GLDAS NOAH), (b) Budyko curve representing the relationship between precipitation (P), potential**
 199 **evapotranspiration (PET) and actual transpiration (AET). The points above the water limit (blue line) indicate the**
 200 **contribution of soil moisture to ET. The seasons (points) above the energy limit (red line) indicate the precipitation loss**
 201 **by infiltration. The plots represent observations corresponding to Autumn of 2000 to Summer of 2019. Each data point**
 202 **represents one season and are color coded by climate of the study areas. See section 3.1 for a description of the data**
 203 **sets used.**

204 Figure 2 shows correlations between the model input data, such as variable climatic or hydrologic cycle metrics (i.e.,
 205 precipitation and evapotranspiration) and vegetation cover for the climate of each study area investigated. The relationships
 206 shown for each area in different climate-ecological zones are based on the 20 years of data used (i.e., Autumn of 2000 –
 207 Summer of 2019). The relationship between fractional vegetation cover (V) and evapotranspiration (ET) indicates a slightly
 208 positive trend in the semi-arid setting (Fig. 2a). Whereas, the relationship in the Mediterranean setting is a steep positive
 209 gradient, with low vegetation cover (0.4– 0.55) and evapotranspiration (i.e., 50 – 100 mm season⁻¹) in the winter, which
 210 increases in summer (90 – 160 mm season⁻¹) in response to vegetation growth (i.e., V = 0.55 – 0.65). Similar trends in V and
 211 ET is indicated in the humid temperate setting during the summer with V in the range of 0.55 – 0.75 and ET ranging between
 212 150 – 350 mm season⁻¹. However, during winters, even after high V in humid setting, lower values in ET are reported, with a
 213 positive trend. To help understand the datasets of precipitation (P) with ET, a Budyko curve is presented in figure 2b, where
 214 the actual ET (AET) and potential ET (PET) are normalized by P. In figure 2b most the data points from the humid temperate

215 setting are above the energy limit and indicate high soil water infiltration during summer seasons. Also, data points above the
216 water limit (blue line in Fig. 2b) indicate a carry-over in soil moisture from a wet season to few dry seasons in the humid,
217 Mediterranean and semi-arid settings.

218 3.2 Estimation of runoff rates

219 The precipitation rates [m season^{-1}] are subjected to soil-water infiltration [m season^{-1}] and evapotranspiration [m season^{-1}] to
220 estimate the seasonal runoff rates [mm season^{-1}]. The runoff rates (R) at every time step (t) are calculated using the actual soil-
221 water infiltration (I_a) and the actual evapotranspiration (ET) as follows,

$$222 \quad R(t) = P(t) - I_a(t) - ET(t), \quad (1)$$

223 where, P is the precipitation amount in a season. This relationship was applied in the model grid cells with non-zero sediment
224 thickness. As ET is the input parameter, there may be instances of higher ET than P in the summer seasons in the humid,
225 Mediterranean and semi-arid settings. This is evident in figure 2b where the minimum of both values is used as ET in the given
226 time-step.

227 The soil-water infiltration rate was estimated by applying the Green-Ampt equation (Green and Ampt, 1911; Julien et al.,
228 1995):

$$229 \quad f(t) = K_e \left(1 + \frac{\psi \cdot \Delta\theta}{F} \right), \quad (2)$$

230 where $f(t)$ is the infiltration rate [m s^{-1}] at time t , K_e is the effective hydraulic conductivity [m s^{-1}], F is the cumulative infiltration
231 [m], Ψ is the suction at the wetting front [m], and $\Delta\theta$ is the difference between saturated and initial volumetric moisture content
232 [$\text{m}^3 \text{m}^{-3}$]. Effective hydraulic conductivity is highly variable and anisotropic; hence, it was considered to be uniform with a
233 value of $1 \times 10^{-6} \text{ m s}^{-1}$ for each catchment.

234 Following the approach of Istanbuluoglu and Bras, (2006) for loamy soils, the soil-water infiltration was modified to account
235 for variable vegetation cover in each grid cell, as follows:

$$236 \quad I_c(t) = f(t)(1 - V(t)) + 4f(t)(V(t)), \quad (3)$$

$$237 \quad I_a(t) = \text{Min}[P(t), I_c(t)], \quad (4)$$

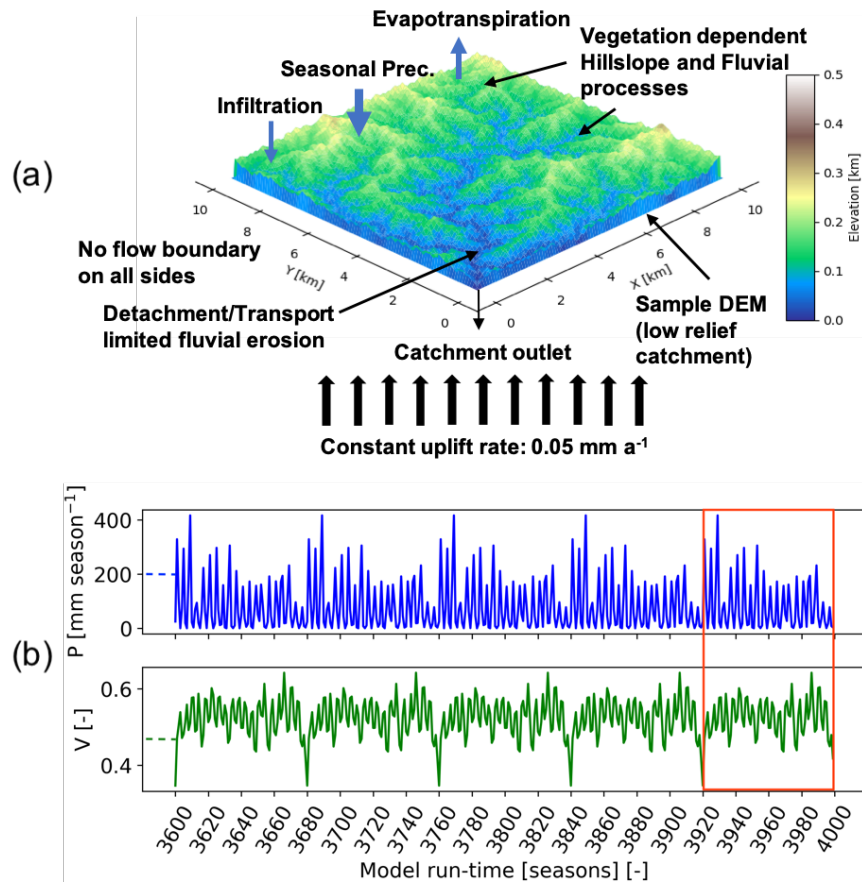
238 where I_c is the infiltration capacity and V is the vegetation cover (between 0 and 1) in a model grid cell at time-step t . Values
239 used in the simulations for the parameters in equations 2-4 are provided in appendix Table A1.

240 3.3 Model setup

241 We applied the Landlab landscape evolution model, a python-based modeling toolkit (Hobley et al., 2017), combined with the
242 SPACE 1.0 model (Shobe et al., 2017). The SPACE model allows coupled detachment-transport limited fluvial processes with
243 simultaneous bedrock erosion and sediment entrainment/deposition. The Landlab-SPACE programs were applied using a set
244 of runtime scripts and input files (Sharma and Ehlers, 2023) to account for vegetation and climate change effects on catchment
245 erosion (i.e., fluvial erosion and hillslope diffusion), using the approach described in Schmid et al. (2018) and Sharma et al.
246 (2021). In addition, the geomorphic processes considered involve weathering and regolith production (Barnhart et al., 2019)
247 and infiltration of surface water into soil (Rengers et al., 2016) based on the Green-Ampt method (Green and Ampt, 1911),
248 and runoff modeling.

249 The model parameters (Table. A1) are selected for the distinct climate and ecological settings in the Chilean Coastal Cordillera
250 based on the observations presented in Schaller et al., (2018). The model state parameters (i.e., erodibility, diffusivity, rock
251 uplift rate, etc.) in the simulations are adapted from Sharma et al., (2021). The model was simulated at a seasonal scale (time
252 step of three months) from the autumn of 2000 (01/03/2000) to the summer of 2019 (28/02/2020). Simulations were conducted

253 for a total time of 1000 years with a time-step of 1 season (3 months) with 20 years (2000 – 2019) of observations in vegetation
 254 and precipitation. These 20-years of observations were repeated (looped) 50 times, to identify, and detrend, long-term transient
 255 trends in catchment erosion rates due to potential differences in actual and assumed erosional parameters such as the hillslope
 256 diffusivity or fluvial erodibility. The combined effects of temporally variable (at seasonal scale) precipitation and vegetation
 257 cover (also spatially variable) on catchment-scale erosion rates are therefore the primary factors influencing predicted erosion
 258 rates.



259
 260 **Figure 3. Schematic of the model geometry and seasonal precipitation and vegetation forcings used in this study. (a)**
 261 **Model setup representing sample DEM (low relief catchment) with no flow boundaries on all sides and a single**
 262 **catchment outlet. The model involves vegetation-dependent seasonal hillslope and fluvial processes and rainfall-**
 263 **infiltration-runoff modeling. (b) Seasonal precipitation and vegetation cover dataset (Mediterranean, La Campana,**
 264 **setting) for the last five iterations of model simulations. The results of highlighted iterations (after detrending for long-**
 265 **term transients) are analyzed in consecutive sections.**

266 **3.4 Boundary and initial conditions**

267 The boundaries are closed (no flow) on all sides, with a single stream outlet at the point of minimum elevation at boundary
 268 nodes (Fig. 3). Initial sediment cover thickness is considered uniform across the model domain, and was approximated based
 269 on observations by Schaller et al., (2018) and Dal Bo et al., (2019). The sediment thickness used are 0.2 m in the arid (AZ),
 270 0.45 m in semi-arid (SG), 0.6 m in the Mediterranean (LC), and 0.7 m in humid temperate (NA) catchments. The rock uplift
 271 rate is kept constant throughout the entire model run as 0.05 mm yr^{-1} , adapted from a similar study (Sharma et al., 2021).

272 **3.5 Overview of simulations conducted**

273 The simulations were designed to identify the sensitivity of erosion rates to seasonal variations in either precipitation rates or
 274 vegetation cover, as well as the more realistic scenario of coupled seasonal variations in both vegetation cover and

275 precipitation. We evaluated this sensitivity with a step-wise increase in model complexity. Three sets of simulations were
276 designed for the four selected study areas, which are as follows,

- 277 1. Scenario 1: Influence of constant (mean seasonal) precipitation with seasonal variations in vegetation cover
278 catchment-scale erosion rates.
- 279 2. Scenario 2: Influence of seasonal variation in precipitation and constant (mean seasonal) vegetation cover on
280 catchment-scale erosion rates.
- 281 3. Scenario 3: Influence of coupled seasonal variations in both precipitation and vegetation cover on catchment-scale
282 erosion rates.

283 The results for scenarios 1 – 3 are illustrated in sections 4.1, 4.2, and 4.3, respectively.

284 **3.6 Detrending of results for long term transients**

285 Model simulations were conducted for 1,000 years using 20 years [March-2000 – Feb-2020] of observations in vegetation
286 cover, and precipitation and were repeated 50 times for a total simulation duration of 1000 years. Simulations presented here
287 were conducted on the present-day topography to allow for the application of observed time series of precipitation and
288 vegetation change in different ecosystems and study areas. This choice of setting comes with the compromise that the erosional
289 parameters (e.g., diffusivity, erodibility, etc.) used in the model are likely not the same as those that led to the present-day
290 catchment topography. As a result, a long-term transient in erosion rates is expected as the model tries to reach an equilibrium
291 with assumed erosional parameters. To correct for any long-term transients in erosion influencing our interpretations, we
292 conducted a linear detrending of the results to remove any long-term variations. The detrending was conducted through a linear
293 regression over entire time series of 1000 years and the values were corrected using the slope of the regression line. Hence,
294 the detrended model results for the last 20 years were analyzed and discussed in sections 4 and 5. In practice, the detrending
295 of time series did not impart a significant change to the results presented.

296 **4 Results**

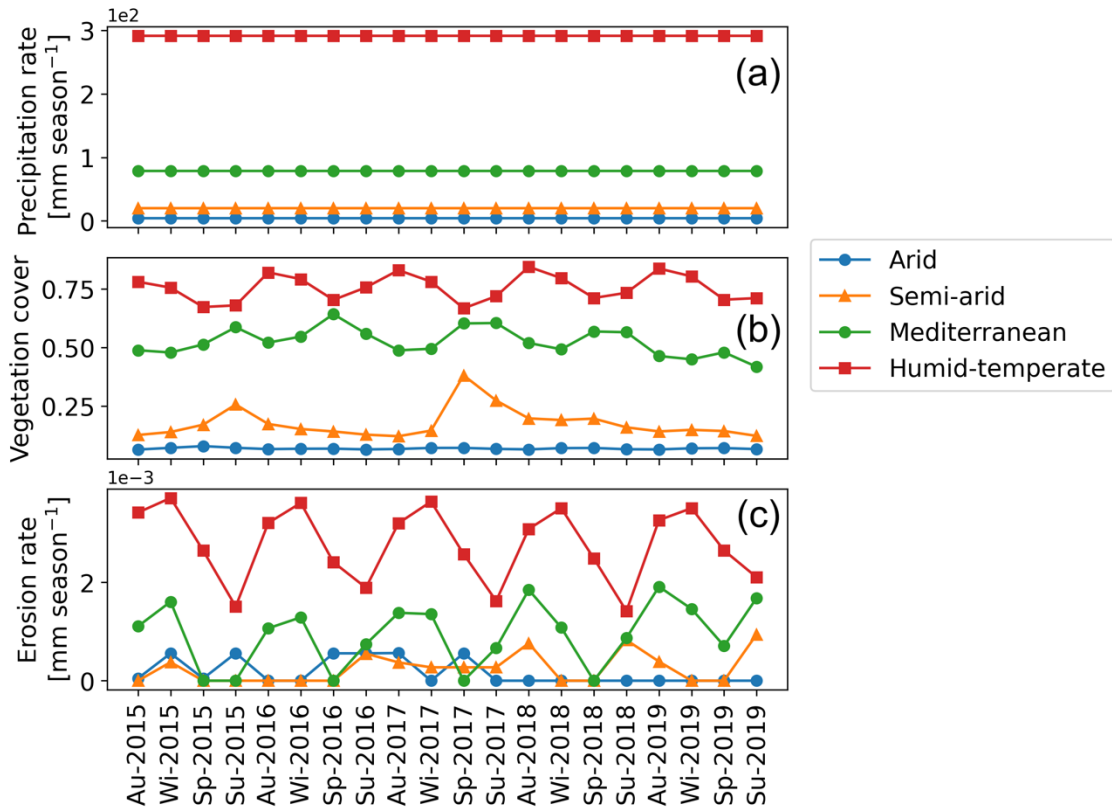
297 In the following sections, we focus our analysis on the mean catchment erosion rates over seasonal (3 months) time scales (see
298 Table. 1). In all scenarios, the rock uplift rate was kept constant at 0.05 mm yr^{-1} following the approach of Sharma et al. (2021).
299 For simple representation, the results of the last five years of the last cycle of transient simulations starting from Autumn-2015
300 to Summer-2019 are displayed in Fig. 4, 6, and 8 (after detrending, see section 3.6). The results for the entire time series
301 (Autumn-2000 – Summer-2019) are available in the supplement (Fig. 1 – 3). The precipitation and erosion rates are shown
302 with the units [mm season^{-1}].

303 **4.1 Scenario 1: Influence of constant precipitation and seasonal variations in vegetation cover on erosion rates**

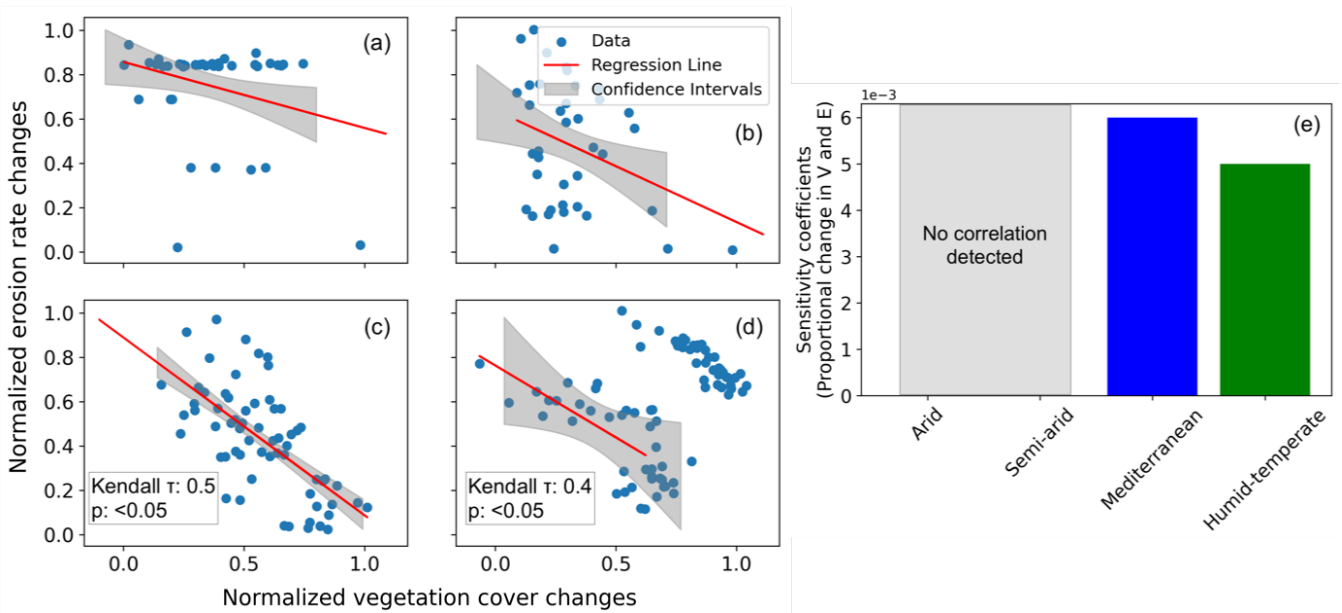
304 In scenario 1, vegetation cover (MODIS NDVI from March 2000 to February 2020) fluctuates seasonally (Fig. 4b), and
305 precipitation rates are kept constant at the seasonal mean (i.e., MAP divided by the number of seasons in a year) during the
306 entire time-series (Fig. 4a) (Ziese et al., 2020). The range of seasonal vegetation cover variations (and mean seasonal
307 precipitation rates) are observed as $0.06 - 0.08$ ($3.92 \text{ mm season}^{-1}$), $0.1 - 0.4$ ($20.16 \text{ mm season}^{-1}$), $0.35 - 0.65$ ($79 \text{ mm season}^{-1}$),
308 and $0.5 - 0.85$ ($292 \text{ mm season}^{-1}$) for the arid, semi-arid, Mediterranean and, humid temperate settings, respectively (Figs.
309 4a-b). The predicted mean catchment seasonal erosion rates range between $0 - 6 \times 10^{-4} \text{ mm season}^{-1}$, $0 - 9.4 \times 10^{-4} \text{ mm}$
310 season^{-1} , $0 - 2.3 \times 10^{-3} \text{ mm season}^{-1}$, and $1.2 \times 10^{-3} - 4 \times 10^{-3} \text{ mm season}^{-1}$ for the arid, semi-arid, Mediterranean and
311 humid temperate settings, respectively (Fig. 4c).

312 To analyze the relationships between the relative changes in forcings and responses, seasonal changes in vegetation cover and
313 erosion rates were normalized between 0 and 1 and plotted in Figs. 5a-d. An inverse relationship and negative correlation

314 (Kendall-tau correlation coefficient: 0.4 – 0.5) is visible between the normalized catchment erosion rates and vegetation cover
 315 for the dry season and wet season separately in the humid temperate (Fig. 5d) and Mediterranean settings (Fig. 5c). The linear
 316 relationship in vegetation and erosion change in the Mediterranean and humid-temperate settings indicates that these
 317 catchments are dominated by fluvial (water driven) and overland flow processes, and the role of hillslope diffusion is minimal.
 318 In contrast, no correlation was found for the arid and semi-arid settings.



319
 320 **Figure 4. Results of simulations with constant seasonal precipitation and variable vegetation over last 5 years (Autumn-**
 321 **2015 – Summer-2019) of last cycle of transient-state model run representing: (a) mean catchment seasonal precipitation**
 322 **rates [mm season⁻¹], (b) mean catchment seasonal vegetation cover [-], and (c) mean catchment seasonal erosion rates**
 323 **[mm season⁻¹].**



324
 325 **Figure 5. Seasonal changes (normalized) in vegetation cover and erosion rates for the scenario with constant**
 326 **precipitation and seasonal changes in vegetation cover in (a) arid, (b) semi-arid, (c) Mediterranean, and (d) humid-**

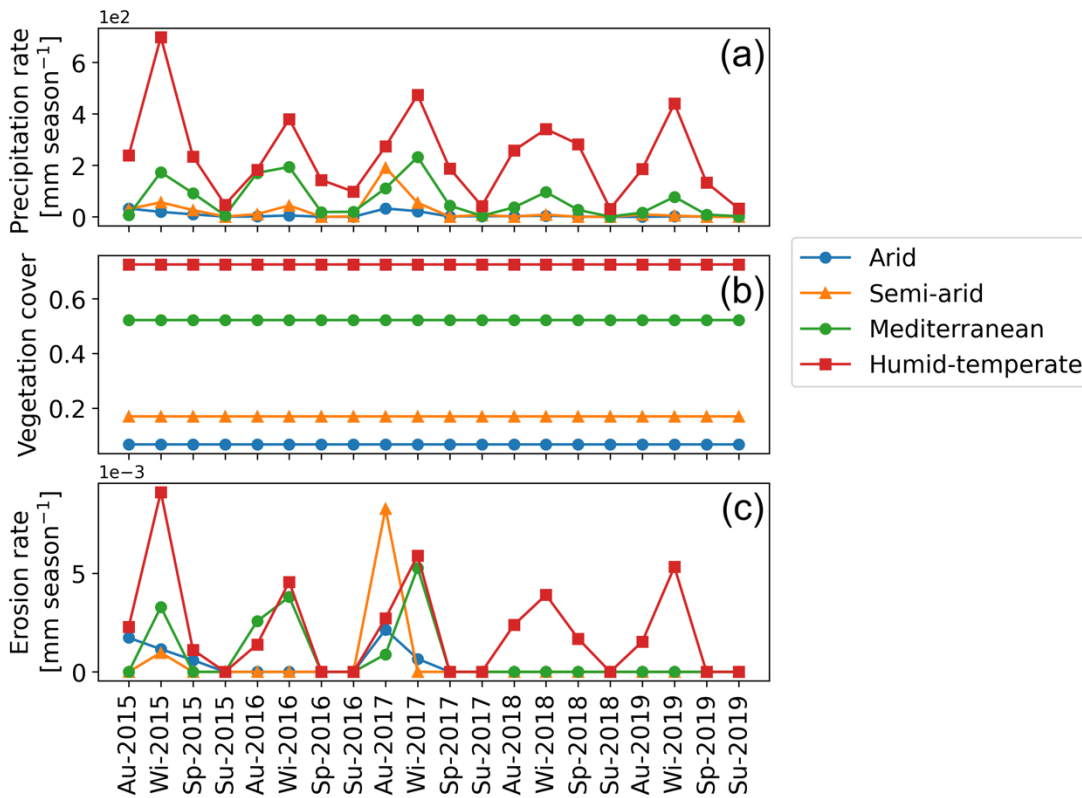
327 temperate settings, with the information on confidence interval (grey shading) and Kendall-tau correlation coefficients.
 328 (e) Sensitivity coefficients for proportional changes in vegetation cover and erosion rates based on the slope and
 329 intercept of the regression lines for the above environmental settings. The sensitivity coefficient is defined as the slope
 330 of the regression line presented in sub-sections a-d.

331 The sensitivity coefficients based on slope and intercept of the regression lines (Figs. 5a-d) are plotted in Fig. 5e. The results
 332 indicate a higher sensitivity of erosion rates to seasonal vegetation changes in the Mediterranean setting relative to humid-
 333 temperate setting. However, in the arid and semi-arid settings, the lack of a significant correlation in the change in vegetation
 334 cover and erosion rates leads to a low sensitivity. This is owed to very low mean precipitation rates ($<20 \text{ mm season}^{-1}$) in the
 335 arid and semi-arid settings. The predicted erosion rates are relatively low (e.g., $<0.004 \text{ mm season}^{-1}$) in this scenario, due to
 336 low mean precipitation rates, which are primarily subjected to infiltration and evapotranspiration in these drier settings.

337 4.2 Scenario 2: Influence of seasonal variations in precipitation and constant vegetation cover on erosion rates

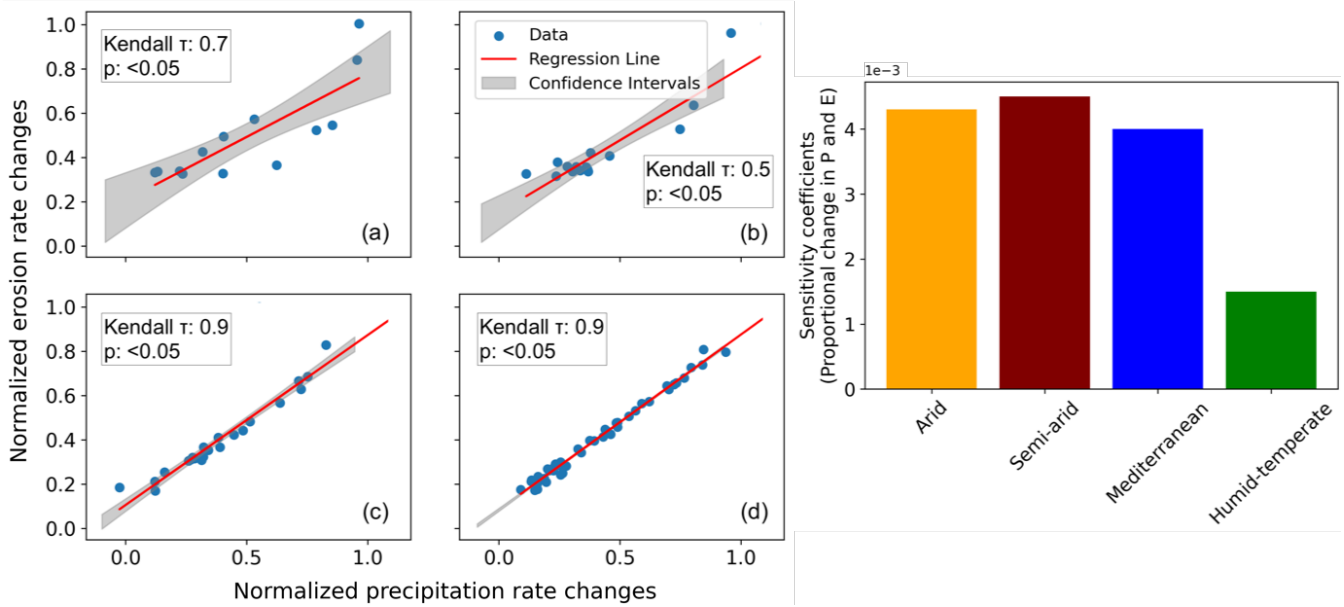
338 In scenario 2, vegetation cover (MODIS NDVI from Mar-2000 – Feb-2020) is kept constant at the mean seasonal vegetation
 339 cover (Fig. 6b) and precipitation rates vary seasonally (Mar-2000 – Feb-2020) (Fig. 6a). The range of seasonal precipitation
 340 rate variations are observed in the range of $0 - 32.42 \text{ mm season}^{-1}$, $0 - 191.66 \text{ mm season}^{-1}$, $0.03 - 417 \text{ mm season}^{-1}$, and $26 -$
 341 $987 \text{ mm season}^{-1}$ in the arid, semi-arid, Mediterranean and, humid temperate settings, respectively.

342 The simulated mean catchment seasonal erosion rates are observed in the range of $0 - 2 \times 10^{-3} \text{ mm season}^{-1}$, $0 - 8.3 \times 10^{-3}$
 343 mm season^{-1} , $0 - 1.37 \times 10^{-2} \text{ mm season}^{-1}$, and $0 - 1.3 \times 10^{-2} \text{ mm season}^{-1}$ in the arid, semi-arid, Mediterranean and, humid
 344 temperate settings, respectively (Fig. 6c).



345
 346 **Figure 6. Results of simulations with variable seasonal precipitation and constant vegetation over last 5 years (Autumn-**
 347 **2015 – Summer-2019) of last cycle of transient-state model run representing: (a) mean catchment seasonal precipitation**
 348 **rates [mm season⁻¹], (b) mean catchment seasonal vegetation cover [-], and (c) mean catchment seasonal erosion rates**
 349 **[mm season⁻¹].**

350 Similar to scenario 1, the changes in seasonal precipitation and erosion rates were normalized between 0 and 1 and plotted in
 351 Figs. 7a-d. A strong positive correlation (Kendall-tau correlation coefficient ranging from 0.5 in semi-arid to 0.9 in
 352 Mediterranean and humid-temperate settings) in the normalized precipitation and erosion rates changes is predicted with the
 353 majority of the data points within the 95% confidence interval in all the settings. The sensitivity coefficients based on the
 354 proportional changes in precipitation and erosion rates, indicate the highest sensitivity in semi-arid settings) with ~5%, ~11%
 355 and ~67% lower sensitivities in the arid, Mediterranean, and humid-temperate settings, respectively (Fig. 7e). This may be
 356 owed to the occasional El Niño events with extremely high precipitation occurring in the arid and semi-arid settings (with
 357 sparse vegetation cover).



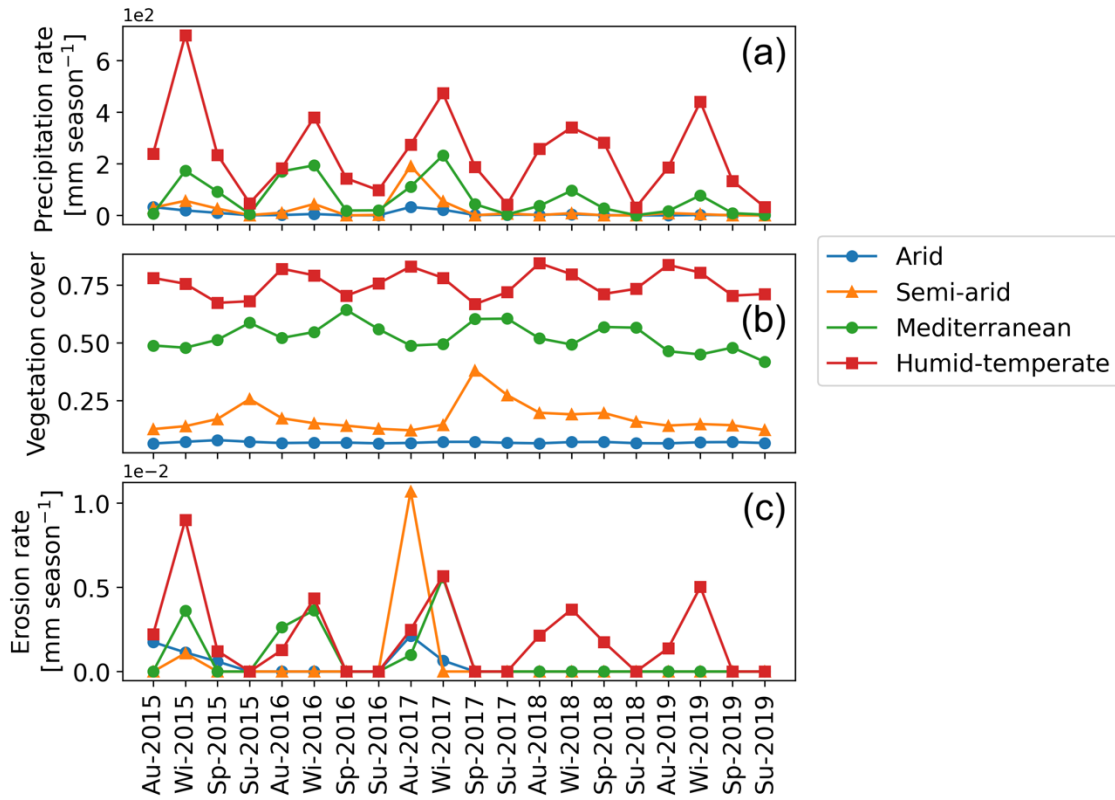
358
 359 **Figure 7. Seasonal changes (normalized) in precipitation and erosion rates for the scenario with seasonal changes in**
 360 **precipitation rates and constant vegetation cover in (a) arid, (b) semi-arid, (c) Mediterranean, and (d) humid-temperate**
 361 **settings, with the information on confidence interval (grey shading) and Kendall-tau correlation coefficients. (e)**
 362 **Sensitivity coefficients for proportional changes in precipitation and erosion rates based on the slope and intercept of**
 363 **the regression lines for the above environmental settings. The sensitivity coefficient is defined as the slope of the**
 364 **regression line presented in sub-sections a-d.**

365 4.3 Scenario 3: Influence of coupled seasonal variations in both precipitation and vegetation cover on erosion rates

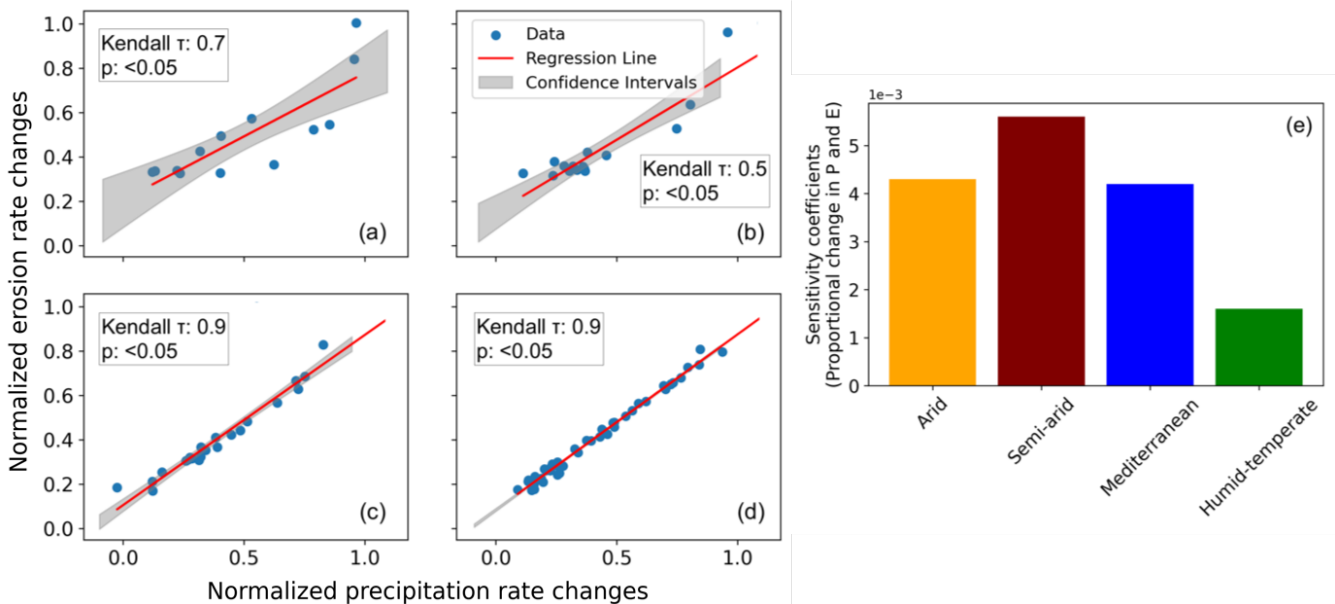
366 In this scenario, coupled variations in seasonal vegetation cover (MODIS NDVI from Mar-2000 – Feb-2020) (Fig. 8b) and
 367 precipitation rates are presented for the years 2000 - 2019 (Fig. 8a). The range of seasonal precipitation rates (and seasonal
 368 vegetation cover, V) variations are 0 – 32.42 mm season⁻¹ (V= 0.06 – 0.08), 0 – 191.66 mm season⁻¹ (0.1 – 0.38), 0.03 – 417
 369 mm season⁻¹ (0.35 – 0.65), and 26 – 987 mm season⁻¹ (0.5 – 0.85) in the arid, semi-arid, Mediterranean and, humid temperate
 370 settings, respectively (Figs. 8a-b). The mean catchment seasonal erosion rates range between 0 – 2 × 10⁻³ mm season⁻¹, 0 –
 371 1 × 10⁻² mm season⁻¹, 0 – 1.4 × 10⁻² mm season⁻¹, and 0 – 1.4 × 10⁻² mm season⁻¹ in the arid, semi-arid, Mediterranean
 372 and, humid temperate settings, respectively (Fig. 8c).

373 Changes in precipitation on erosion rates were normalized between 0 and 1 and plotted in figures. 9a-d. Similar to the results
 374 from scenario 2, a strong positive correlation was predicted in all the environmental settings. The sensitivity coefficients based
 375 on the proportional changes in precipitation and erosion rates, indicate the highest sensitivity in the semi-arid settings with
 376 ~25% and ~71% lower sensitivities in arid and Mediterranean, and humid-temperate settings, respectively (Fig. 9e). Similarly,
 377 the isolated effect of changes the in the vegetation cover on erosion rates (Fig. 10) does not yield a significant correlation in
 378 arid, semi-arid and Mediterranean settings. However, we observe a strong negative correlation in the humid-temperate setting

379 (Fig. 10d) during the wet season (Kendall tau correlation coefficient: -0.6, with >95% significance level). Hence, the sensitivity
 380 coefficients in this case are not plotted.
 381 The similarity in results obtained from scenarios 2 and 3 suggest a first-order control of seasonal precipitation changes on
 382 erosion rates (~70% higher sensitivity to changes in precipitation), with less significance to vegetation cover changes. For
 383 example, the sensitivity of erosion to precipitation rate changes in semi-arid setting is predicted as ~70% higher to that of
 384 humid-temperate setting in both the scenarios.
 385

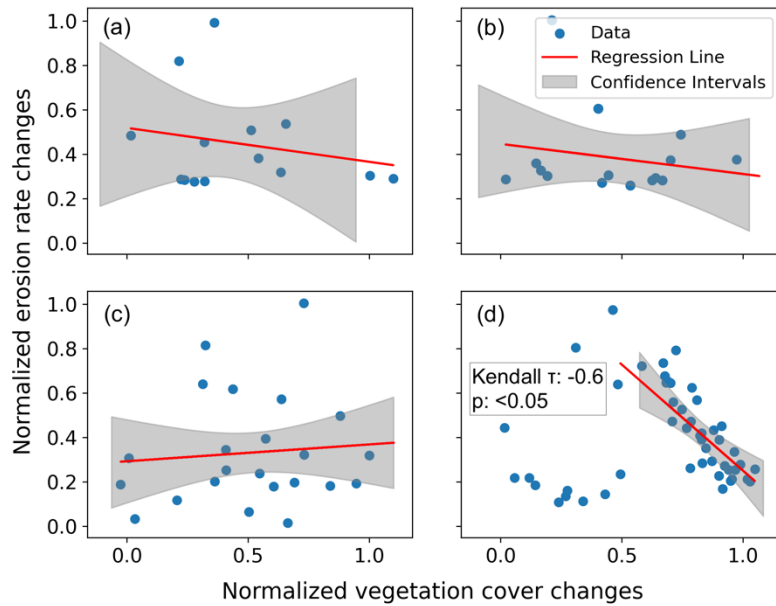


386
 387 **Figure 8. Results of simulations with coupled variations in seasonal precipitation and vegetation over the last five years**
 388 **(Autumn-2015 – Summer-2019) of the last cycle of transient-state model run representing: (a) mean catchment seasonal**
 389 **precipitation rates [mm season⁻¹], (b) mean catchment seasonal vegetation cover [-], and (c) mean catchment seasonal**
 390 **erosion rates [mm season⁻¹].**



392 **Figure 9. Seasonal changes (normalized) in precipitation and erosion rates for the scenario with coupled seasonal**
 393 **changes in both precipitation rates and vegetation cover in (a) arid, (b) semi-arid, (c) Mediterranean, and (d) humid-**
 394 **temperate settings, with the information on confidence interval (grey shading) and Kendall-tau correlation coefficients.**
 395 **(e) Sensitivity coefficients for proportional changes in precipitation and erosion rates based on the slope and intercept**
 396 **of the regression lines for the above environmental settings. The sensitivity coefficient is defined as the slope of the**
 397 **regression line presented in sub-sections a-d.**

398



399

400 **Figure 10. Seasonal changes (normalized) in vegetation cover and erosion rates for the scenario with coupled seasonal**
 401 **changes in both precipitation rates and vegetation cover in (a) arid, (b) semi-arid, (c) Mediterranean, and (d) humid-**
 402 **temperate settings, with the information on confidence interval (grey shading) and Kendall-tau correlation coefficients.**

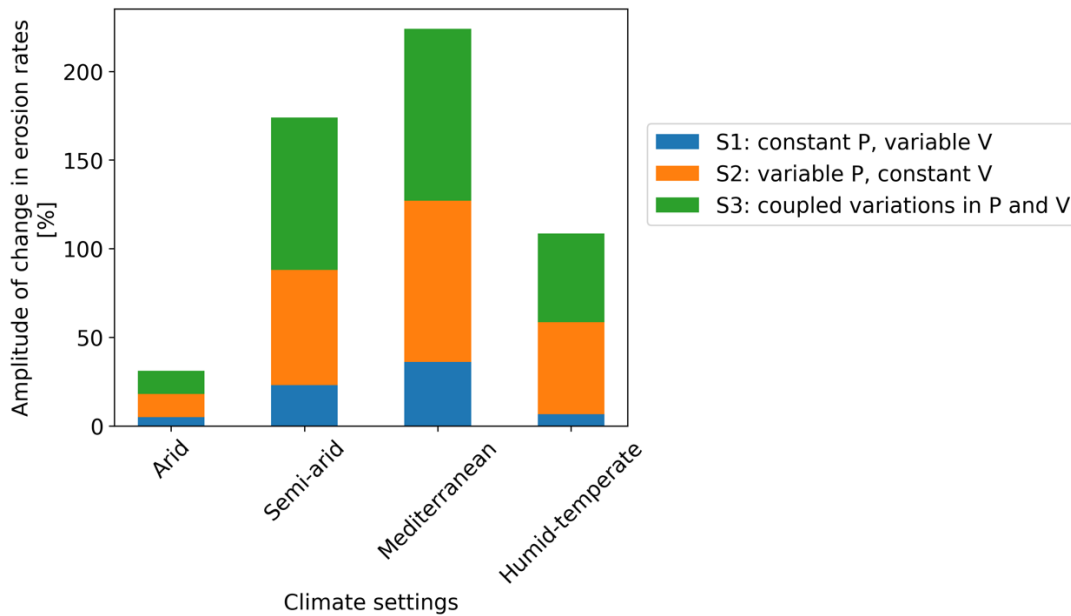
403 5 Discussion

404 This section discusses the relationship between variations in seasonal precipitation and vegetation cover with erosion rates in
 405 the form of the amplitude of change for each model scenario (section 5.1). This is followed by the synthesis of catchment scale
 406 erosion rates variability over wet and dry seasons (section 5.2). In section 5.3, we discuss the impact transient dynamics of
 407 sediment transport in our modelling approach. Finally, we compare our results with previously published studies (section 5.4)
 408 and discuss model limitations (section 5.5).

409 5.1 Synthesis of the amplitude of change in erosion rates for model scenarios 1-3

410 The amplitude of change of mean catchment erosion rates [in percentage] varies at a seasonal scale (Fig. 11) between the study
 411 areas. The amplitude of change in erosion rates to their respective mean values was estimated (Fig. 11) using the coefficient
 412 of variation in percent (standard deviation divided by the mean of a dataset). The coefficient of variation is a statistical tool to
 413 compare multiple variables free from scale effects. It is a dimensionless quantity (Brown, 1998). This comparison represents
 414 the sensitivity of each catchment to changing seasonal weather for all three model scenarios (sections 4.1 – 4.3).

415 In scenario 1, with seasonal variations in vegetation cover and constant seasonal precipitation (Fig. 11), the amplitude of
 416 change in erosion rates ranges between 5% in the arid and 36% in Mediterranean setting. The above results support the findings
 417 of Zhang et al. (2019), which observed 20-30% of the total change in sediment yield with constant precipitation and variable
 418 vegetation cover. The above study used the soil and water assessment tool (SWAT) based on NDVI and climate parameters.



419

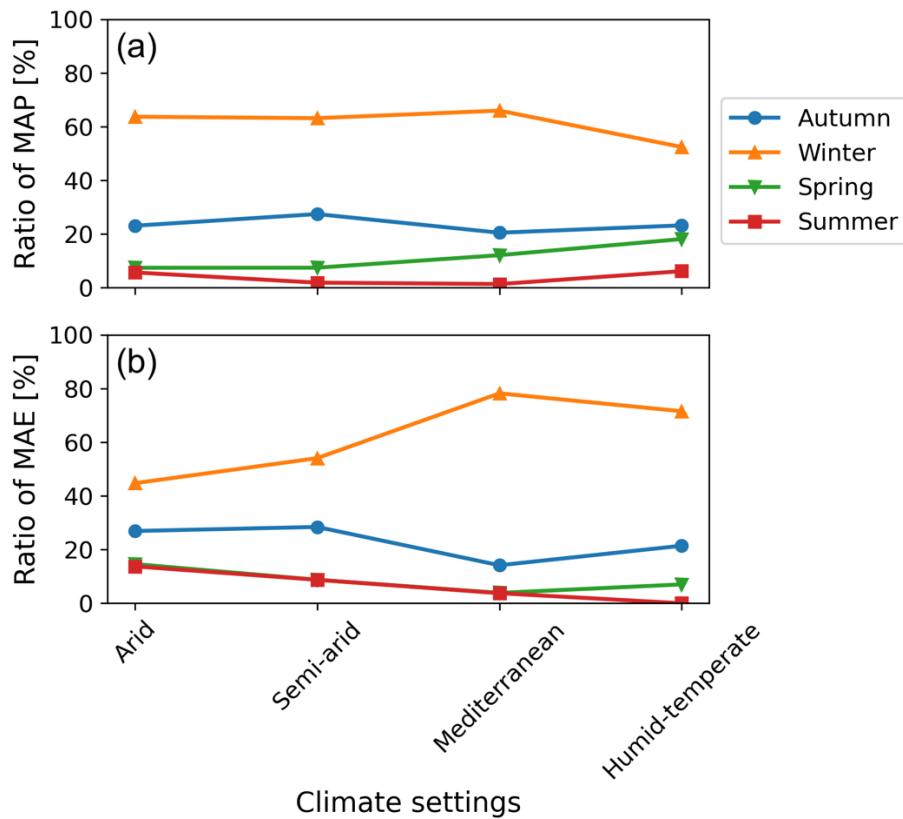
420 **Figure 11. Stacked bar plot depicting the amplitude of change in seasonal erosion rates (relative to their respective**
 421 **means). Scenario 1 is shown in blue and had variable vegetation cover and constant precipitation rates. Scenario 2 is**
 422 **shown in orange and had constant vegetation cover and variable precipitation rates, and scenario 3 is shown in green**
 423 **and represents the simulation with coupled variations in vegetation cover and precipitation rates.**

424 In scenario 2, with constant vegetation cover and variable precipitation rates (Fig. 11), the amplitude of change in erosion rates
 425 ranges from 13% in the arid setting (AZ) to 52%, 65%, and 91% in humid-temperate (NA), semi-arid (SG) and Mediterranean
 426 (LC) settings, respectively. A similar trend is observed in scenario 3 with coupled variations in vegetation cover and
 427 precipitation rates (Fig. 11), with the amplitude of change in erosion rates between 13% in the arid setting up to 50%, 86%,
 428 and 97% in the humid-temperate, semi-arid and Mediterranean settings, respectively. The magnitude of erosion rate changes
 429 is amplified in scenario 3, especially in the semi-arid setting (e.g., ~21% increase in the amplitude of change from scenario 2
 430 to scenario 3). This amplification could be owed to the 35% change in vegetation cover in the semi-arid setting (Fig. 8).
 431 Overall, these observations indicate a high sensitivity of erosion in semi-arid and Mediterranean environments compared to
 432 arid and humid-temperate settings.

433 The pattern of erosion rate changes in scenarios 1-3 implies a dominant control of precipitation variations (rather than
 434 vegetation cover change) on catchment erosion rates at a seasonal scale. This interpretation is consistent with previous
 435 observational studies. For example, a field study by Suescún et al. (2017) in the Columbian Andes highlighted the significant
 436 influence of precipitation seasonality (over vegetation cover seasonality) on runoff and erosion rates. An observational
 437 catchment-scale study in the semi-arid Chinese Loess Plateau by Wei et al. (2015) indicated that intra-annual precipitation
 438 variations were a significant contributor to monthly runoff and sediment yield variations.

439 5.2 Synthesis of catchment erosion rates over wet and dry seasons

440 In this section, we discuss the ratio of seasonal precipitation and erosion rates with the mean annual precipitation (MAP) (Fig.
 441 12a) and mean annual erosion (MAE) (Fig. 12b) during different seasons (i.e., autumn – summer) in a year, averaged over the
 442 last cycle of the transient simulations (i.e., depicting the erosion rate predictions for 2000 – 2019). These are defined as the
 443 ratio of the mean erosion (and precipitation) rates in a season (e.g., winter) to the mean annual erosion rates (and MAP) during
 444 the last 20 years of the transient simulations. This was done to identify the impact of precipitation during wet seasons (in this
 445 case, winter) in influencing the annual erosion rates. This analysis was performed for the simulation results of scenario 3 for
 446 different climate and ecological settings (i.e., arid to humid-temperate). We do this specifically with scenario 3 results to
 447 capture the trends in erosion rates with coupled variations in model input (i.e., precipitation and vegetation cover).



448

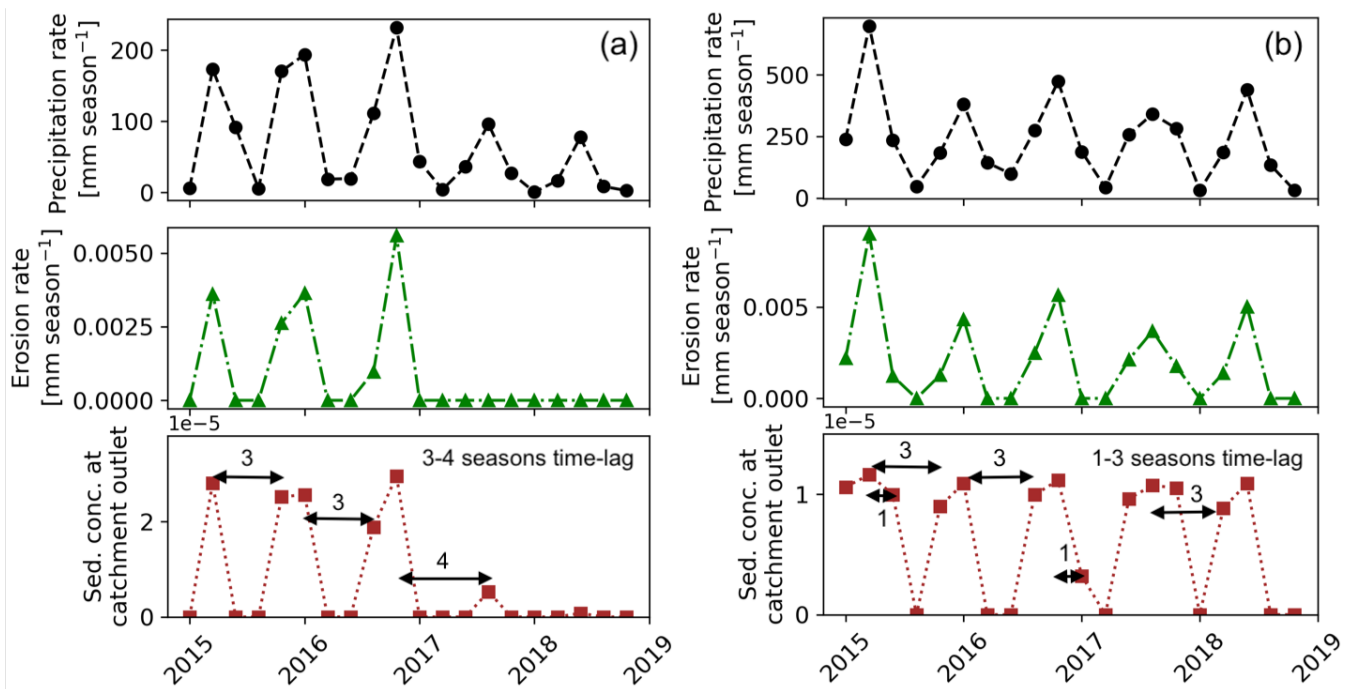
449 **Figure 12. The ratio of seasonal precipitation and erosion rates to mean annual precipitation (MAP) and mean annual**
 450 **erosion (MAE) during the last cycle of transient simulations results from scenario 3 (coupled seasonal variations in**
 451 **precipitation and vegetation cover). The plots correspond to (a) the ratio of MAP per season [%] and (b) ratio of MAE**
 452 **per season [%]. Each color and point style represent the ratio for a distinct climate setting i.e., arid, semi-arid,**
 453 **Mediterranean, and humid-temperate settings.**

454 The values for the ratio of MAP during different seasons (Fig. 12a) depicts winter (June-August) and summer (December-
 455 February) as the wettest and driest seasons of the year, respectively. For example, all study areas receive >50% and <6% of
 456 MAP during winters and summers. The same is reflected in Fig. 12b with 45%, 55%, 78%, and 71% of MAE in the arid, semi-
 457 arid, Mediterranean, and humid-temperate settings, respectively, during winters. On the contrary, during summers the share of
 458 MAE decreases from 14% in the arid setting to 1% in the humid-temperate setting. The Autumn (March-May) receives lower
 459 precipitation amounts that range from 20–30% of MAP in the study areas. Arid and semi-arid settings experience a relatively
 460 higher share of MAE (e.g., ~30%) than the Mediterranean and humid temperate settings (e.g., ~15-20%). The Spring season
 461 experiences relatively higher erosion rates despite a smaller share of MAP in arid and semi-arid settings. For example, the arid
 462 and semi-arid settings experience 10-14% of the MAE for ~7% of MAP. At the same time, the Mediterranean and humid-
 463 temperate settings experience 5-7% of MAE for ~12-18% of MAP during Spring. Overall, we find that arid and semi-arid
 464 settings experience <15% and ~50% of MAE during the wet (winter) and dry (summer) seasons. The above relationship is
 465 amplified for the Mediterranean and humid-temperate settings with <5% and >70% of MAE occurring during wet and dry
 466 seasons, respectively. The latter is in agreement with an observational study by Mosaffaie et al., (2015) in a Mediterranean
 467 catchment in Iran. More specifically, Mosaffaie et al., (2015) used field observations from 2012-2013 to conclude that
 468 maximum erosion rates (>70%) are observed during the wet season, which decreases in the dry season (<10%).

469 5.3 Consideration of transient sediment dynamics in model results

470 This section discusses the impact of lag times from when sediment is eroded in a source area until it leaves the catchment
 471 outlet. This analysis was conducted because in natural systems, when sediment is eroded from its source, it takes time to leave

472 the catchment (in this case the model domain) and recorded as eroded in our analysis. According to field studies and modeling
 473 experiments, this time lag is usually more than a season (3 months) (e.g., Buendia et al., (2016)). To capture these time-lags
 474 in precipitation, erosion and concentration of sediment leaving the catchment outlet, the model output for the Mediterranean
 475 and humid-temperate settings are compared (Fig. 13). We perform this analysis on the simulation results of scenario 3 with
 476 coupled variations in seasonal precipitation and vegetation cover. The concentration of sediment is defined as a dimensionless
 477 quantity (Q_s/Q) estimated from sediment flux (Q_s) and discharge rates (Q).



478
 479 **Figure 13. Simulation results (scenario 3: coupled variations in precipitation in vegetation cover) to capture the time-**
 480 **lags in precipitation, erosion rates and sediment concentration at catchment outlet) over the last five years (Autumn-**
 481 **2015 – Summer-2019) of the last cycle of transient-state model run for the catchments in: (a) Mediterranean and (b)**
 482 **humid-temperate setting.**

483 In the Mediterranean settings, these time lags range from 3 to 4 seasons, and are relatively large (e.g., from wet season 2016
 484 to wet season of 2017, see Fig. 13a). However, in humid-temperate setting, these time lags range from 1 to 3 seasons, mostly
 485 owed to the relatively higher precipitation magnitude and frequency in this region (Fig. 13b). In the catchments in both these
 486 climate settings, the pulse of sediment leaving the catchment is fairly distributed with the maximum concentration of sediment
 487 leaving the catchment in the same wet season when it is eroded from its source. These time-lags would result in enhanced
 488 sensitivity of the proportional changes in erosion rates to the changes in seasonal precipitation and (or) vegetation cover, as
 489 the sediment is transported even in the seasons when the sediment is not eroded from its source (e.g., wet season in 2017 in
 490 both the above climate settings). This poses a limitation to the current study and is again revisited in the model limitations
 491 (section 5.5).

492 5.4 Comparison to previous studies

493 In this section, we relate the broad findings of this study to the previously published observational studies. In an observational
 494 study in an agrarian drainage basin in the Belgian Loam Belt, Steegen et al., (2000) evaluated sediment transport over various
 495 time scales (including seasonal). They observed lower sediment fluxes during the seasons with high vegetation cover. In
 496 addition, an observational study by Zheng (2006) investigated the effect of vegetation changes on soil erosion in the Loess
 497 Plateau, China, and concluded that soil erosion was significantly reduced (up to ~50%) after vegetation restoration. Another
 498 observational study in semi-arid grasslands in the Loess Plateau, China, by Hou et al., (2020) highlighted a considerable

499 reduction in erosion rates due to the development of richness and evenness of the plant community in the early to the mid wet
500 season. Our results from scenario 1 (seasonal variations in vegetation cover with constant precipitation rates) support the
501 findings of the above studies whereby a negative correlation (Kendal τ : -0.4 – -0.5) was found between vegetation cover and
502 erosion rates in humid-temperate and Mediterranean settings (see Fig. 5).

503 A catchment-scale observational study in Baspa Valley, NW Himalayas (Wulf et al., 2010), analyzed seasonal precipitation
504 gradients and their impact on fluvial erosion using weather station observations (1998 – 2007). The study observed a positive
505 correlation between precipitation and sediment yield variability, demonstrating the summer monsoon's first-order control on
506 erosion processes. An observational study by Wei et al., (2015) in Loess Plateau, China, evaluated erosion and sediment
507 transport under various vegetation types and precipitation variations. They found that significant changes in landscape pattern
508 and vegetation coverage (i.e., land use land cover) might contribute to long-term dynamics of soil loss. However, seasonal
509 variations in runoff and sediment yield were mainly influenced by rainfall seasonality. In comparison to the results of this
510 study, we find the similarity in the patterns of erosion rates in scenario 2 (variable precipitation and constant vegetation cover)
511 and scenario 3 (coupled variations in precipitation and vegetation) are consistent with the findings of Wei et al., (2015). For
512 example, the amplitude of change in erosion rates (Fig. 10) in scenarios 2 and 3 differ by 0%, 6%, and -2% in the arid,
513 Mediterranean, and humid-temperate settings, respectively. However, this difference is enhanced in the semi-arid region (i.e.,
514 ~23%) due to a relatively high degree of variation (~25%) in seasonal vegetation cover change.

515 Finally, an observational study in the Columbian Andes by Suescún et al., (2017) assessed the impact of seasonality on
516 vegetation cover and precipitation and found higher erosion rates in regions with steeper slopes. Another study by Chakrapani
517 (2005) emphasized the direct impact of local relief and channel slope on sediment yield in natural rivers. The broad findings
518 of the above studies agree with our results from scenarios 1-3, as we find higher erosion rates in the Mediterranean and humid-
519 temperate regions with steeper topography (mean slope ~20 deg), which encounter high seasonality (and intensity) in
520 precipitation.

521 **5.5. Model Limitations**

522 The model setup used in this study was designed to quantify the sensitivity of erosion rates in different climate and ecological
523 settings with variations in precipitation rates and vegetation cover at seasonal scales. We represent the degree of variations in
524 erosion rates in terms of changes in the amplitude (with respect to the mean) for different model scenarios (see sections 4.1 –
525 4.3).

526 Our modeling approach used several simplifying assumptions that warrant discussion and are avenues for investigation in
527 future studies. For example, model results presented here successfully capture the major surface processes, including
528 vegetation-dependent erosion and infiltration, sediment transport, and surface runoff. However, groundwater flow is not
529 considered in the current study, and how the reentry of groundwater into streams over seasonal scales would influence
530 downstream erosion. The reason is that groundwater flow modeling includes a high amount of heterogeneity and anisotropy
531 and requires much finer grid sizes (<1m) and smaller time steps (in seconds to hours). Thus, due to the large grid-cell size (90
532 m), timescales (monthly), and high uncertainty in subsurface hydrologic parameters we were unable to evaluate the effects of
533 groundwater flow on our results. Furthermore, this study assumed uniform lithologic and hydrologic parameters (e.g., vertical
534 hydraulic conductivity, initial soil moisture, evapotranspiration, erodibility, etc.) over the entire catchment. As said earlier,
535 these properties are subject to a high level of uncertainty and heterogeneity, the best fitting parameters, based on previously
536 published literature (e.g., Schaller et al., 2018; Bernhard et al., 2018; Schmid et al., 2018; Sharma et al., 2021) are used for the
537 model simulations. However, the heterogeneity in vegetation cover and related soil-water infiltration per grid cell is used in
538 this study. For the heterogeneity in vegetation cover, we use MODIS-derived NDVI as a proxy of vegetation cover. According
539 to Garatuza-Payán et al. (2005), NDVI is assumed as an effective tool for estimating seasonal changes in vegetation cover
540 density. However, the spatial resolution (250 m) of the NDVI dataset is lower than that of the SRTM DEM (90 m) used in the

541 study. Nevertheless, the difference in spatial resolution of vegetation cover and topography might introduce ambiguity in the
542 model results. Furthermore, transient dynamics associated with sediment storage in the model is not incorporated in the study
543 to capture the time lag required for the eroded sediment to move out of the model domain. As the LEM (SPACE 1.0) used in
544 this study shuffles between detachment- and transport-limited fluvial erosion, we suspect that in such short timescales (3
545 months) and in small catchments, detachment-limited fluvial erosion is dominant. Hence, any sediment removed from its
546 source is transported out of the domain in a given time-step. However, it is recommended for future studies considering larger
547 or lower gradient catchments, where sediment storage may be more significant than documented here, an analysis of erosion
548 at a local scale (e.g., at individual model grid cells) is recommended.

549 A final limitation stems from several generalized model parameters (e.g., rock uplift rate, erodibility, diffusivity, etc.) applied
550 to the SRTM DEM (as initial topography). We did this to capture the effects of seasonality in precipitation and vegetation
551 cover in modern times (2000 - 2019). However, the current topography might not have evolved with the same tectonic and
552 lithological parameters. To address this limitation, we conducted simulations for 50 iterations and detrended the model results
553 to remove those transient effects (see section 3.6). This limitation can be handled in future studies by parameterizing the model
554 to the current topography using stochastic (e.g., Bayesian) techniques (e.g., Stephenson et al., 2006; Avdeev et al., 2011). As
555 this study was aimed to capture the control of seasonal precipitation and (or) vegetation changes on the relative variability of
556 erosion rates, the above limitation may not pose a problem in the model results.

557 **6 Summary and Conclusions**

558 In this study, we applied a landscape evolution model to quantify the impact of seasonal variations in precipitation and
559 vegetation on catchment averaged erosion rates. We performed this in regions with varied climate and ecology including: arid,
560 semi-arid, Mediterranean, and humid-temperate settings. Three sets of simulations were designed to model erosion rates for
561 (a) scenario 1: constant precipitation and variable vegetation cover, (b) scenario 2: variable precipitation and constant
562 vegetation cover, and (c) scenario 3: coupled variations in precipitation and vegetation cover. The main conclusions derived
563 from this study are as follows:

- 564 1. Scenario 1, with variable vegetation cover and constant precipitation (Fig. 4), resulted in small variations in seasonal
565 erosion rates ($<0.02 \text{ mm yr}^{-1}$) in comparison to the other scenarios. The amplitude of change in seasonal erosion rates
566 (relative to the mean) is the smallest in humid-temperate setting and maximum in the Mediterranean setting (Fig.
567 10a). For example, it ranges from 5% in the arid setting (Pan de Azúcar) to 23% and 36% in the semi-arid (Santa
568 Gracia) and Mediterranean settings (La Campana), respectively.
- 569 2. Scenario 2, with constant vegetation cover and variable precipitation (Fig. 6), results in relatively higher seasonal
570 erosion rates ($<0.06 \text{ mm yr}^{-1}$) in comparison to scenario 1. The amplitude of change in seasonal erosion rates (relative
571 to the mean) is smallest in the arid setting and largest in the Mediterranean setting (Fig. 10b). For example, it ranges
572 from 13% in the arid setting (Pan de Azúcar) to 52%, 65%, and 91% in the humid-temperate (Nahuelbuta), semi-arid
573 (Santa Gracia), and Mediterranean settings (La Campana), respectively.
- 574 3. Scenario 3, with coupled variations in vegetation cover and precipitation (Fig. 8), results in similar seasonal erosion
575 rates ($<0.06 \text{ mm yr}^{-1}$) to scenario 2. Similarly, the amplitude of change in seasonal erosion rates (relative to the mean)
576 is the smallest in the arid setting and the largest in the Mediterranean setting (Fig. 10c). For example, it ranges from
577 13% in the arid setting (Pan de Azúcar) to 50%, 86%, and 97% in the humid-temperate (Nahuelbuta), semi-arid (Santa
578 Gracia), and Mediterranean settings (La Campana), respectively. A significant increase (from scenario 2) in the
579 variation in erosion rates ($\sim 21\%$) is owed to the $\sim 25\%$ variation in vegetation cover in semi-arid settings.
- 580 4. All study areas experience maximum and minimum erosion during wet and dry seasons, respectively (Fig. 11b).
581 However, the difference (in maximum and minimum) is amplified from the arid ($\sim 30\%$) to the Mediterranean and

humid-temperate settings (~70-75%). This is owed to the range of amplitude of precipitation rate change (Fig. 7) increasing from the arid (e.g., ~9 mm) to humid-temperate settings (e.g., ~543 mm) in wet and dry seasons.

Finally, this study was motivated by testing the hypotheses that (1) if precipitation variations primarily influence seasonal erosion, then the influence of seasonal vegetation cover changes would be less significant, and (2) catchment erosion in drier settings is more sensitive to seasonality in precipitation and vegetation, than wetter settings. With respect to hypothesis 1, we found that seasonal precipitation variations primarily drive catchment erosion and the effects of vegetation cover variations are secondary. Results presented here (Fig. 10b) support this interpretation with a high amplitude of change in erosion rates (with respect to means) ranging from 13 to 91% for the scenario with constant vegetation cover and seasonal precipitation variations. However, the effect of seasonal vegetation cover changes is also significant (Fig. 10a), ranging between 5 – 36%. Hence, the first hypothesis is partially confirmed, but the magnitude of response depends on the ecological zone investigated. Concerning hypothesis 2, we found that seasonal changes in catchment erosion are more pronounced in the semi-arid and Mediterranean settings and less pronounced in the arid and humid temperate settings. This interpretation is supported by Fig. 10c, with a significantly high amplitude of change in catchment erosion in semi-arid (~86%) and Mediterranean (~97%) settings with relatively lower changes in humid temperate (~50%) and arid (~13%) settings, partially confirming the hypothesis.

611 **Table A1. Input parameters with corresponding units for the landscape evolution model**

Model Parameters	Values
Grid spacing (dx)	90 m
Model runtime (totalT)	1000 years (2000 - 2019 repeated over 50 times)
time-step (dt)	1 season (3 months)
Rock uplift rate (U) ¹	1.25 x 10 ⁻⁵ [m season ⁻¹] (or 0.05 [mm a ⁻¹])
Initial sediment thickness (H _{initial}) ²	20 (A*), 45 (SA*), 60 (M*), 70 (HT*) [cm]
Bedrock erodibility (Kr) ¹	2 x 10 ⁻⁹ [m ⁻¹]
Sediment erodibility (Ks) ¹	2 x 10 ⁻⁸ [m ⁻¹]
Reach scale bedrock roughness (H*) ¹	1 [m]
Porosity (Φ) ⁴	0.51 (A*), 0.43 (SA*), 0.51 (M*), 0.7 (HT*) [-]
Fraction of fine sediments (Ff) ¹	0.2 [-]
Effective terminal settling velocity (Vs) ¹	2.5 [mm season ⁻¹]
m, n ¹	0.6, 1 [-]
Bedrock erosion threshold stream power (ω _{cr}) ¹	1.25 x 10 ⁻⁵ [m season ⁻¹]
Sed. entr. threshold stream power (ω _{cs}) ¹	1.25 x 10 ⁻⁶ [m season ⁻¹]
Bare soil diffusivity (K _b) ¹	2.5 x 10 ⁻⁴ [m ² season ⁻¹]
Exponential decay coefficient (α) ¹	0.3 [-]
Critical channel formation area (A _{crit}) ³	1 x 10 ⁶ [m ²]
Reference vegetation cover (V _r) ³	1 (100%)
Manning's number for bare soil (n _s) ³	0.01 [-]
Manning's number for ref. vegetation (n _v) ³	0.6 [-]
Scaling factor for vegetation influence (w) ³	1 [-]
Soil bulk density (B) ⁴	1300 (A*), 1500 (SA*), 1300 (M*), 800 (HT*) [kg m ⁻³]
Soil type ⁴	sandy loam (A*, SA*, and M*); sandy clay loam (HT*)
Initial soil moisture (s) ⁵	0.058 (A*), 0.02 (SA*), 0.053 (M*), 0.15 (HT*) [m ³ m ⁻³]

612 ¹Sharma et al. (2021), ²Schaller et al. (2018), ³Schmid et al. (2018), ⁴Bernhard et al. (2018), ⁵Übernicker et al. (2020).

613 *A: arid; SA: semi-arid; M: Mediterranean; HT: humid-temperate setting.

614 **Appendix B: Implementation of vegetation dependent hillslope and Fluvial processes in Landlab components**615 This section includes the description of vegetation dependent hillslope and fluvial processes defined in the Landlab components
616 used in this study, based on the approaches by Istanbuluoglu (2005) Schmid et al., (2018), and Sharma et al., (2021).617 **B1 Vegetation dependent hillslope processes**

618 The rate of change in topography due to hillslope diffusion (Fernandes and Dietrich, 1997) is defined as follows:

619
$$\frac{\partial z}{\partial t}(\text{hillslope}) = \nabla q_s, \quad (\text{A1})$$

620 where q_s is sediment flux along the slope S . We applied slope and depth-dependent linear diffusion rule following the approach
621 of Johnstone and Hilley (2014) such that:

622
$$q_s = K_d S d_* (1 - e^{-H/d_*}), \quad (\text{A2})$$

623 where K_d is diffusion coefficient [m² yr⁻¹], d_* is sediment transport decay depth [m], and H denotes sediment thickness.

624 The diffusion coefficient is defined as a function of vegetation cover present on hillslopes, which is estimated following the
 625 approach of Istanbuluoglu (2005), as follows:

$$626 \quad K_d = K_b e^{-(\alpha V)}, \quad (A3)$$

627 where K_d is defined as a function of vegetation cover V , an exponential decay coefficient α , and linear diffusivity K_b for bare
 628 soil.

629 **B2 Vegetation dependent fluvial processes**

630 The fluvial erosion is estimated for a two-layer topography (i.e., bedrock and sediment are treated explicitly) in the coupled
 631 detachment- / transport-limited model, SPACE 1.0 (Shobe et al., 2017). Bedrock erosion and sediment entrainment are
 632 calculated simultaneously in the model. Total fluvial erosion is defined as:

$$633 \quad \frac{\partial z}{\partial t} (\text{fluvial}) = \frac{\partial R}{\partial t} + \frac{\partial H}{\partial t}, \quad (A4)$$

634 where, left-hand side denotes the total fluvial erosion rate. The first and second terms on right-hand side denote the bedrock
 635 erosion rate and sediment entrainment rate.

636 The rate of change of height of bedrock R per unit time [m yr^{-1}] is defined as:

$$637 \quad \frac{\partial R}{\partial t} = U - E_r, \quad (A5)$$

638 where E_r [m yr^{-1}], is the volumetric erosion flux of bedrock per unit bed area.

639 The change in sediment thickness H [m] per unit time [yr] is defined as a fraction net deposition rate and solid fraction
 640 sediments, as follows:

$$641 \quad \frac{\partial H}{\partial t} = \frac{D_s - E_s}{1 - \phi}, \quad (A6)$$

642 where, D_s [m yr^{-1}] is the deposition flux of sediment, E_s [m yr^{-1}] is volumetric sediment entrainment flux per unit bed area, and
 643 ϕ is the sediment porosity.

644 Following the approach of Shobe et al. (2017), E_s and E_r given by:

$$645 \quad E_s = (K_s q^m S^n - \omega_{cs}) \left(1 - e^{-\frac{H}{H_*}} \right), \quad (A7)$$

$$646 \quad E_r = (K_r q^m S^n - \omega_{cr}) e^{-H/H_*}, \quad (A8)$$

647 where, K_s [m^{-1}] and K_r [m^{-1}] are the sediment erodibility and bedrock erodibility parameters respectively. The threshold stream
 648 power for sediment entrainment and bedrock erosion are denoted as ω_{cs} [m yr^{-1}] and ω_{cr} [m yr^{-1}] in above equations. Bedrock
 649 roughness is denoted as H_* [m] and the term e^{-H/H_*} corresponds to the soil production from bedrock. With higher bedrock
 650 roughness magnitudes, more sediment would be produced.

651 K_s and K_r were modified in the model runtime scripts by introducing the effect of Manning's roughness to quantify the effect
 652 of vegetation cover on bed shear stress in each model cell:

$$653 \quad \tau_v = \rho_w g (n_s + n_v)^{6/10} q^m S^n F_t, \quad (A9)$$

654 where, ρ_w [kg m^{-3}] and g [m s^{-2}] are the density of water and acceleration due to gravity respectively. Manning's numbers for
 655 bare soil and vegetated surface are denoted as n_s and n_v . F_t represents shear stress partitioning ratio. Manning's number for
 656 vegetation cover and F_t are calculated as follows:

$$657 \quad n_v = n_{vr} \left(\frac{V}{V_r} \right)^w, \quad (A10)$$

$$F_t = \left(\frac{n_s}{n_s + n_v} \right)^{\frac{3}{2}}, \quad (\text{A11})$$

where, n_{vr} is Manning's number for the reference vegetation. Here, V_r is reference vegetation cover ($V = 100\%$) and V is local vegetation cover in a model cell, w is empirical scaling factor.

By combining stream power equation (Tucker et al., 1999; Howard, 1994; Whipple and Tucker, 1999) and above concept of the effect of vegetation on shear stress, we follow the approach of Schmid et al. (2018) and Sharma et al. (2021) to define new sediment and bedrock erodibility parameters influenced by the surface vegetation cover on fluvial erosion, as follows:

$$K_{vs} = K_s \rho_w g (n_s + n_v)^{6/10} F_t, \quad (\text{A12})$$

$$K_{vr} = K_r \rho_w g (n_s + n_v)^{6/10} F_t, \quad (\text{A13})$$

where, K_{vs} [m^{-1}] and K_{vr} [m^{-1}] are modified sediment erodibility and bedrock erodibility respectively. These are influenced by the effect of presence of fraction of vegetation cover V . Hence, K_s and K_r in Eq. (8) and Eq. (9) are replaced by K_{vs} and K_{vr} to include an effect of vegetation cover on fluvial processes in the model. The trends of K_d , K_{vs} and K_{vr} are illustrated in Fig. 3 in Sharma et al., (2021).

Code and data availability

The code and data used in this study are freely available via Zenodo (<https://doi.org/10.5281/zenodo.8033782>, Sharma and Ehlers, 2023).

Author contributions

HS and TAE designed the initial model setup and simulation programs. HS and TAE conducted model modifications, simulation runs, and analysis. HS prepared the paper with contributions from TAE.

Competing interests

The authors declare that they have no conflict of interest.

Acknowledgments

We acknowledge the support from the Open Access Publishing fund of the University of Tübingen. We would like to thank two anonymous reviewers and Omer Yetemen for their constructive reviews. We also thank Simon Mudd for editing this paper.

Financial support

This research has been supported by the Deutsche Forschungs Gemeinschaft (grant nos. EH329/14-2, SPP-1803, and Research Training Group 1829 Integrated Hydrosystem Modelling).

Review Statement

This paper was edited by Simon Mudd and reviewed by two anonymous reviewers and Omer Yetemen.

- 688 Avdeev, B., Niemi, N. A., and Clark, M. K.: Doing more with less: Bayesian estimation of erosion models with detrital
689 thermochronometric data, *Earth Planet. Sci. Lett.*, 305, 385–395, <https://doi.org/10.1016/j.epsl.2011.03.020>, 2011.
- 690 Barnhart, K. R., Glade, R. C., Shobe, C. M., and Tucker, G. E.: Terrainbento 1.0: a Python package for multi-model analysis
691 in long-term drainage basin evolution, *Geosci. Model Dev.*, 12, 1267–1297, <https://doi.org/10.5194/gmd-12-1267-2019>,
692 2019.
- 693 Beaudoin, H., Rodell, M., and NASA/GSFC/HSL: GLDAS Noah Land Surface Model L4 monthly 0.25 x 0.25 degree,
694 Version 2.1, <https://doi.org/10.5067/SXAVCZFAQLNO>, 2020.
- 695 Bernhard, N., Moskwa, L.-M., Schmidt, K., Oeser, R. A., Aburto, F., Bader, M. Y., Baumann, K., von Blanckenburg, F.,
696 Boy, J., van den Brink, L., Brucker, E., Büdel, B., Canessa, R., Dippold, M. A., Ehlers, T. A., Fuentes, J. P., Godoy, R.,
697 Jung, P., Karsten, U., Köster, M., Kuzyakov, Y., Leinweber, P., Neidhardt, H., Matus, F., Mueller, C. W., Oelmann, Y.,
698 Oses, R., Osses, P., Paulino, L., Samolov, E., Schaller, M., Schmid, M., Spielvogel, S., Spohn, M., Stock, S., Stroncik, N.,
699 Tielbörger, K., Übernickel, K., Scholten, T., Seguel, O., Wagner, D., and Kühn, P.: Pedogenic and microbial interrelations to
700 regional climate and local topography: New insights from a climate gradient (arid to humid) along the Coastal Cordillera of
701 Chile, *CATENA*, 170, 335–355, <https://doi.org/10.1016/j.catena.2018.06.018>, 2018.
- 702 Bookhagen, B., Thiede, R. C., and Strecker, M. R.: Abnormal monsoon years and their control on erosion and sediment flux
703 in the high, arid northwest Himalaya, *Earth Planet. Sci. Lett.*, 231, 131–146, <https://doi.org/10.1016/j.epsl.2004.11.014>,
704 2005.
- 705 Brown, C. E.: Coefficient of Variation, in: *Applied Multivariate Statistics in Geohydrology and Related Sciences*, Springer,
706 Berlin, Heidelberg, 1998.
- 707 Buendia, C., Vericat, D., Batalla, R. J., and Gibbins, C. N.: Temporal Dynamics of Sediment Transport and Transient In-
708 channel Storage in a Highly Erodible Catchment: LINKING SEDIMENT SOURCES, RAINFALL PATTERNS AND
709 SEDIMENT YIELD, *Land Degrad. Dev.*, 27, 1045–1063, <https://doi.org/10.1002/ldr.2348>, 2016.
- 710 Carretier, S., Tolorza, V., Regard, V., Aguilar, G., Bermúdez, M. A., Martinod, J., Guyot, J.-L., Hérail, G., and Riquelme,
711 R.: Review of erosion dynamics along the major N-S climatic gradient in Chile and perspectives, *Geomorphology*, 300, 45–
712 68, <https://doi.org/10.1016/j.geomorph.2017.10.016>, 2018.
- 713 Cerdà, A.: The influence of aspect and vegetation on seasonal changes in erosion under rainfall simulation on a clay soil in
714 Spain, *Can. J. Soil Sci.*, 78, 321–330, <https://doi.org/10.4141/S97-060>, 1998.
- 715 Chakrapani, G. J.: Factors controlling variations in river sediment loads, *Curr. Sci.*, 88, 569–575, 2005.
- 716 Deal, E., Favre, A. C., and Braun, J.: Rainfall variability in the Himalayan orogen and its relevance to erosion processes:
717 RAINFALL VARIABILITY IN THE HIMALAYAS, *Water Resour. Res.*, 53, 4004–4021,
718 <https://doi.org/10.1002/2016WR020030>, 2017.
- 719 Didan, Kamel: MOD13Q1 MODIS/Terra Vegetation Indices 16-Day L3 Global 250m SIN Grid V006,
720 <https://doi.org/10.5067/MODIS/MOD13Q1.006>, 2015.
- 721 Earth Resources Observation And Science (EROS) Center: Shuttle Radar Topography Mission (SRTM) Void Filled,
722 <https://doi.org/10.5066/F7F76B1X>, 2017.
- 723 Fernandes, N. F. and Dietrich, W. E.: Hillslope evolution by diffusive processes: The timescale for equilibrium adjustments,
724 *Water Resour. Res.*, 33, 1307–1318, <https://doi.org/10.1029/97wr00534>, 1997.
- 725 Ferreira, V. and Panagopoulos, T.: Seasonality of Soil Erosion Under Mediterranean Conditions at the Alqueva Dam
726 Watershed, *Environ. Manage.*, 54, 67–83, <https://doi.org/10.1007/s00267-014-0281-3>, 2014.
- 727 Gabarrón-Galeote, M. A., Martínez-Murillo, J. F., Quesada, M. A., and Ruiz-Sinoga, J. D.: Seasonal changes in the soil
728 hydrological and erosive response depending on aspect, vegetation type and soil water repellency in different Mediterranean
729 microenvironments, *Solid Earth*, 4, 497–509, <https://doi.org/10.5194/se-4-497-2013>, 2013.
- 730 Gao, P., Li, Z., and Yang, H.: Variable discharges control composite bank erosion in Zoige meandering rivers, *CATENA*,
731 204, 105384, <https://doi.org/10.1016/j.catena.2021.105384>, 2021.

- 732 Garatuza-Payán, J., Sánchez-Andrés, R., Sánchez-Carrillo, S., and Navarro, J. M.: Using remote sensing to investigate
733 erosion rate variability in a semiarid watershed, due to changes in vegetation cover, *IAHS Publ.*, 292, 144–151, 2005.
- 734 Glodny, J., Gräfe, K., Echtler, H., and Rosenau, M.: Mesozoic to Quaternary continental margin dynamics in South-Central
735 Chile (36–42°S): the apatite and zircon fission track perspective, *Int. J. Earth Sci.*, 97, 1271–1291,
736 <https://doi.org/10.1007/s00531-007-0203-1>, 2008.
- 737 Green, W. H. and Ampt, G. A.: Studies on Soil Physics., *J. Agric. Sci.*, 4, 1–24, <https://doi.org/10.1017/S002185960001441>,
738 1911.
- 739 Hancock, G. and Lowry, J.: Hillslope erosion measurement—a simple approach to a complex process, *Hydrol. Process.*, 29,
740 4809–4816, 2015.
- 741 Hancock, G. and Lowry, J.: Quantifying the influence of rainfall, vegetation and animals on soil erosion and hillslope
742 connectivity in the monsoonal tropics of northern Australia, *Earth Surf. Process. Landf.*, 46, 2110–2123,
743 <https://doi.org/10.1002/esp.5147>, 2021.
- 744 Herrmann, S. M. and Mohr, K. I.: A Continental-Scale Classification of Rainfall Seasonality Regimes in Africa Based on
745 Gridded Precipitation and Land Surface Temperature Products, *J. Appl. Meteorol. Climatol.*, 50, 2504–2513,
746 <https://doi.org/10.1175/JAMC-D-11-024.1>, 2011.
- 747 Hobley, D. E. J., Adams, J. M., Nudurupati, S. S., Hutton, E. W. H., Gasparini, N. M., Istanbuluoglu, E., and Tucker, G. E.:
748 Creative computing with Landlab: an open-source toolkit for building, coupling, and exploring two-dimensional numerical
749 models of Earth-surface dynamics, *Earth Surf. Dyn.*, 5, 21–46, <https://doi.org/10.5194/esurf-5-21-2017>, 2017.
- 750 Hou, J., Zhu, H., Fu, B., Lu, Y., and Zhou, J.: Functional traits explain seasonal variation effects of plant communities on
751 soil erosion in semiarid grasslands in the Loess Plateau of China, *Catena*, v. 194, 104743–,
752 <https://doi.org/10.1016/j.catena.2020.104743>, 2020.
- 753 Howard, A. D.: A detachment-limited model of drainage basin evolution, *Water Resour. Res.* V 30, 2261–2285, 1994.
- 754 Huete, A., Didan, K., Miura, T., Rodriguez, E. P., Gao, X., and Ferreira, L. G.: Overview of the radiometric and biophysical
755 performance of the MODIS vegetation indices, *Remote Sens. Environ.*, 83, 195–213, [https://doi.org/10.1016/S0034-4257\(02\)00096-2](https://doi.org/10.1016/S0034-4257(02)00096-2), 2002.
- 757 Istanbuluoglu, E.: Vegetation-modulated landscape evolution: Effects of vegetation on landscape processes, drainage
758 density, and topography, *J. Geophys. Res.*, 110, <https://doi.org/10.1029/2004jf000249>, 2005.
- 759 Istanbuluoglu, E. and Bras, R. L.: On the dynamics of soil moisture, vegetation, and erosion: Implications of climate
760 variability and change, *Water Resour. Res.*, 42, 2006.
- 761 Johnstone, S. A. and Hilley, G. E.: Lithologic control on the form of soil-mantled hillslopes, *Geology*, 43, 83–86,
762 <https://doi.org/10.1130/G36052.1>, 2014.
- 763 Julien, P. Y., Saghafian, B., and Ogden, F. L.: RASTER-BASED HYDROLOGIC MODELING OF SPATIALLY-VARIED
764 SURFACE RUNOFF1, *JAWRA J. Am. Water Resour. Assoc.*, 31, 523–536, <https://doi.org/10.1111/j.1752-1688.1995.tb04039.x>, 1995.
- 766 Langbein, W. B. and Schumm, S. A.: Yield of sediment in relation to mean annual precipitation, *Eos Trans. Am. Geophys. Union*, 39, 1076–1084, <https://doi.org/10.1029/TR039i006p01076>, 1958.
- 768 Leyland, J., Hackney, C. R., Darby, S. E., Parsons, D. R., Best, J. L., Nicholas, A. P., Aalto, R., and Lague, D.: Extreme
769 flood-driven fluvial bank erosion and sediment loads: direct process measurements using integrated Mobile Laser Scanning
770 (MLS) and hydro-acoustic techniques: Direct measurement of flood-driven erosion using MLS and MBES, *Earth Surf. Process. Landf.*, 42, 334–346, <https://doi.org/10.1002/esp.4078>, 2016.
- 772 Melnick, D.: Rise of the central Andean coast by earthquakes straddling the Moho, *Nat. Geosci.*, 9, 401–407,
773 <https://doi.org/10.1038/ngeo2683>, 2016.
- 774 Melnick, D., Bookhagen, B., Strecker, M. R., and Echtler, H. P.: Segmentation of megathrust rupture zones from fore-arc
775 deformation patterns over hundreds to millions of years, Arauco peninsula, Chile: EARTHQUAKE SEGMENTATION AT
776 ARAUCO, *J. Geophys. Res. Solid Earth*, 114, <https://doi.org/10.1029/2008JB005788>, 2009.

- 777 Mosaffaie, J., Ekhtesasi, M. R., Dastorani, M. T., Azimzadeh, H. R., and Zare Chahuki, M. A.: Temporal and spatial
778 variations of the water erosion rate, *Arab. J. Geosci.*, 8, 5971–5979, <https://doi.org/10.1007/s12517-014-1628-z>, 2015.
- 779 Oeser, R. A., Stroncik, N., Moskwa, L.-M., Bernhard, N., Schaller, M., Canessa, R., Brink, L. van den, Köster, M., Brucker,
780 E., Stock, S., Fuentes, J. P., Godoy, R., Matus, F. J., Pedraza, R. O., McIntyre, P. O., Paulino, L., Seguel, O., Bader, M. Y.,
781 Boy, J., Dippold, M. A., Ehlers, T. A., Kühn, P., Kuzyakov, Y., Leinweber, P., Scholten, T., Spielvogel, S., Spohn, M.,
782 Übernicker, K., Tielbörger, K., Wagner, D., and Blanckenburg, F. von: Chemistry and microbiology of the Critical Zone
783 along a steep climate and vegetation gradient in the Chilean Coastal Cordillera, *CATENA*, 170, 183–203,
784 <https://doi.org/10.1016/j.catena.2018.06.002>, 2018.
- 785 Rengers, F. K., McGuire, L., Kean, J. W., Staley, D. M., and Hobley, D. E. J.: Model simulations of flood and debris flow
786 timing in steep catchments after wildfire, *Water Resour. Res.*, 52, 6041–6061, <https://doi.org/10.1002/2015WR018176>,
787 2016.
- 788 Rodell, M., Houser, P. R., Jambor, U., Gottschalck, J., Mitchell, K., Meng, C.-J., Arsenault, K., Cosgrove, B., Radakovich,
789 J., Bosilovich, M., Entin, J. K., Walker, J. P., Lohmann, D., and Toll, D.: The Global Land Data Assimilation System, *Bull.*
790 *Am. Meteorol. Soc.*, 85, 381–394, <https://doi.org/10.1175/BAMS-85-3-381>, 2004.
- 791 Schaller, M. and Ehlers, T. A.: Comparison of soil production, chemical weathering, and physical erosion rates along a
792 climate and ecological gradient (Chile) to global observations, *Earth Surf. Dyn.*, 10, 131–150, [https://doi.org/10.5194/esurf-](https://doi.org/10.5194/esurf-10-131-2022)
793 [10-131-2022](https://doi.org/10.5194/esurf-10-131-2022), 2022.
- 794 Schaller, M., Ehlers, T. A., Lang, K. A. H., Schmid, M., and Fuentes-Espoz, J. P.: Addressing the contribution of climate and
795 vegetation cover on hillslope denudation, Chilean Coastal Cordillera (26°–38°S), *Earth Planet. Sci. Lett.*, 489, 111–122,
796 <https://doi.org/10.1016/j.epsl.2018.02.026>, 2018.
- 797 Schaller, M., Dal Bo, I., Ehlers, T. A., Klotzsche, A., Drews, R., Fuentes Espoz, J. P., and van der Kruk, J.: Comparison of
798 regolith physical and chemical characteristics with geophysical data along a climate and ecological gradient, Chilean Coastal
799 Cordillera (26 to 38\degree\,S), *SOIL*, 6, 629–647, <https://doi.org/10.5194/soil-6-629-2020>, 2020.
- 800 Schmid, M., Ehlers, T. A., Werner, C., Hickler, T., and Fuentes-Espoz, J.-P.: Effect of changing vegetation and precipitation
801 on denudation – Part 2: Predicted landscape response to transient climate and vegetation cover over millennial to million-
802 year timescales, *Earth Surf. Dyn.*, 6, 859–881, <https://doi.org/10.5194/esurf-6-859-2018>, 2018.
- 803 Sharma and Ehlers: LandLab investigations into the seasonal effects of precipitation and vegetation change on catchment
804 erosion, , <https://doi.org/10.5281/zenodo.8033782>, 2023.
- 805 Sharma, H., Ehlers, T. A., Glotzbach, C., Schmid, M., and Tielbörger, K.: Effect of rock uplift and Milankovitch timescale
806 variations in precipitation and vegetation cover on catchment erosion rates, *Earth Surf. Dyn.*, 9, 1045–1072,
807 <https://doi.org/10.5194/esurf-9-1045-2021>, 2021.
- 808 Shobe, C. M., Tucker, G. E., and Barnhart, K. R.: The SPACE 1.0 model: A Landlab component for 2-D calculation of
809 sediment transport, bedrock erosion, and landscape evolution, *Geosci. Model Dev. Discuss.*, 1–38,
810 <https://doi.org/10.5194/gmd-2017-175>, 2017.
- 811 Starke, J., Ehlers, T. A., and Schaller, M.: Latitudinal effect of vegetation on erosion rates identified along western South
812 America, *Science*, 367, 1358–1361, <https://doi.org/10.1126/science.aaz0840>, 2020.
- 813 Steegen, A., Govers, G., Nachtergaele, J., Takken, I., Beuselinck, L., and Poesen, J.: Sediment export by water from an
814 agricultural catchment in the Loam Belt of central Belgium, *Geomorphology*, 33, 25–36, [https://doi.org/10.1016/S0169-](https://doi.org/10.1016/S0169-555X(99)00108-7)
815 [555X\(99\)00108-7](https://doi.org/10.1016/S0169-555X(99)00108-7), 2000.
- 816 Stephenson, J., Gallagher, K., and Holmes, C.: A Bayesian approach to calibrating apatite fission track annealing models for
817 laboratory and geological timescales, *Geochim. Cosmochim. Acta*, 70, 5183–5200,
818 <https://doi.org/10.1016/j.gca.2006.07.027>, 2006.
- 819 Suescún, D., Villegas, J. C., León, J. D., Flórez, C. P., García-Leoz, V., and Correa-Londoño, G. A.: Vegetation cover and
820 rainfall seasonality impact nutrient loss via runoff and erosion in the Colombian Andes, *Reg. Environ. Change*, 17, 827–839,
821 <https://doi.org/10.1007/s10113-016-1071-7>, 2017.
- 822 Tucker, G. E. and Bras, R. L.: A stochastic approach to modeling the role of rainfall variability in drainage basin evolution,
823 *Water Resour. Res.*, 36, 1953–1964, <https://doi.org/10.1029/2000wr900065>, 2000.

- 824 Tucker, G. E., Gasparini, N. M., Lancaster, S. T., and Bras, R. L.: Modeling Floodplain Dynamics and Stratigraphy:
825 Implications for Geoarchaeology, 1999.
- 826 Übernicketl, K., Ehlers, T. A., Ershadi, M. R., Paulino, L., Fuentes Espoz, J.-P., Maldonado, A., Osés-Pedraza, R., and von
827 Blanckenburg, F.: Time series of meteorological station data in the EarthShape study areas of in the Coastal Cordillera,
828 Chile, <https://doi.org/10.5880/FIDGEO.2020.043>, 2020.
- 829 Wang, L., Zheng, F., Liu, G., Zhang, X. J., Wilson, G. V., Shi, H., and Liu, X.: Seasonal changes of soil erosion and its
830 spatial distribution on a long gentle hillslope in the Chinese Mollisol region, *Int. Soil Water Conserv. Res.*, 9, 394–404,
831 <https://doi.org/10.1016/j.iswcr.2021.02.001>, 2021.
- 832 Wei, W., Chen, L., Zhang, H., and Chen, J.: Effect of rainfall variation and landscape change on runoff and sediment yield
833 from a loess hilly catchment in China, *Environ. Earth Sci.*, 73, 1005–1016, <https://doi.org/10.1007/s12665-014-3451-y>,
834 2015.
- 835 Whipple, K. X. and Tucker, G. E.: Dynamics of the stream-power river incision model: Implications for height limits of
836 mountain ranges, landscape response timescales, and research needs, *J. Geophys. Res. Solid Earth*, 104, 17661–17674,
837 <https://doi.org/10.1029/1999jb900120>, 1999.
- 838 Wulf, H., Bookhagen, B., and Scherler, D.: Seasonal precipitation gradients and their impact on fluvial sediment flux in the
839 Northwest Himalaya, *Geomorphology*, 118, 13–21, <https://doi.org/10.1016/j.geomorph.2009.12.003>, 2010.
- 840 Yetemen, O., Istanbuluoglu, E., Flores-Cervantes, J. H., Vivoni, E. R., and Bras, R. L.: Ecohydrologic role of solar radiation
841 on landscape evolution, *Water Resour. Res.*, 51, 1127–1157, <https://doi.org/10.1002/2014wr016169>, 2015.
- 842 Zhang, S., Li, Z., Hou, X., and Yi, Y.: Impacts on watershed-scale runoff and sediment yield resulting from synergetic
843 changes in climate and vegetation, *Catena*, 179, 129–138, <https://doi.org/10.1016/j.catena.2019.04.007>, 2019.
- 844 Zhang, W., An, S., Xu, Z., Cui, J., and Xu, Q.: The impact of vegetation and soil on runoff regulation in headwater streams
845 on the east Qinghai–Tibet Plateau, China, *Catena*, 87, 182–189, <https://doi.org/10.1016/j.catena.2011.05.020>, 2011.
- 846 Zhang, X., Yu, G. Q., Li, Z. B., and Li, P.: Experimental Study on Slope Runoff, Erosion and Sediment under Different
847 Vegetation Types, *Water Resour. Manag.*, 28, 2415–2433, <https://doi.org/10.1007/s11269-014-0603-5>, 2014.
- 848 Zheng, F. L.: Effect of Vegetation Changes on Soil Erosion on the Loess Plateau1 1Project supported by the Chinese
849 Academy of Sciences (No. KZCX3-SW-422) and the National Natural Science Foundation of China (Nos. 9032001 and
850 40335050)., *Pedosphere*, 16, 420–427, [https://doi.org/10.1016/S1002-0160\(06\)60071-4](https://doi.org/10.1016/S1002-0160(06)60071-4), 2006.
- 851 Ziese, M., Rauthe-Schöch, A., Becker, A., Finger, P., Rustemeier, E., and Schneider, U.: GPCC Full Data Daily Version
852 2020 at 1.0°: Daily Land-Surface Precipitation from Rain-Gauges built on GTS-based and Historic Data: Gridded Daily
853 Totals (2020), https://doi.org/10.5676/DWD_GPCC/FD_D_V2020_100, 2020.
- 854